Montanuniversität Leoben

Influence of proton irradiation on the precipitation kinetics and mechanical properties of an intermetallic precipitation hardened steel

Diploma thesis

written by

Christina Hofer

This thesis was conducted at the Department of Physical Metallurgy and Materials Testing at the University of Leoben in cooperation with the Nuclear Engineering Department at UC Berkeley.

Leoben, June 2012

Affidavit

I declare in lieu of oath, that I wrote this thesis and performed the associated research myself, using only literature cited in this volume

Leoben, June 2012

Christina Hofer

ACKNOWLEDGEMENT

First of all I want to thank the ‘Marshallplan Jubiläumsstiftung’ and the Montanuniversität Leoben for providing the financial support to perform my diploma thesis in the USA. The time at the University of California, Berkeley, was rewarding on both counts, professionally and personally.

I want to thank Univ.-Prof. Dr. Helmut Clemens for giving me the possibility to conduct this thesis at his department.

My sincere gratitude and appreciation is due to my supervisor Dr. Harald Leitner for his encouragement and support to go abroad, his guidance and extensive discussions for a successful completion of this thesis.

Thank you to Dr. Peter Hosemann for supervising me during my time at UC Berkeley.

I owe my deepest gratitude to Dr. Erich Stergar for his constant support and the fun we had during and besides work. Thank you for your kindness and your friendship.

During this work I have collaborated with many colleagues for whom I have great regard, and I wish to express my warmest thanks to all those who have helped me with my work at the Department of Physical Metallurgy and Materials Testing at the Montanuniversität Leoben and the Department of Nuclear Engineering at UC Berkeley.

Furthermore, it is a pleasure to thank the many great friends I made during my time in Leoben for their kindness and moral support. My special thanks go to Karoline Kormout who has mastered all the ups and downs of the studies with me from the first day on. Thank you, Karo.

Finally I would like to show my deepest gratitude to my family, particularly my parents, for their unconditional support and strong faith in me.

Table of contents

Abbreviations

ATP	**A**tom **p**robe **t**omography
CAES	**C**enter for **A**dvanced **E**nergy **S**tudies
FD	**F**requency **d**istribution
FIM	**F**ield **e**mission **m**icroscope
FIB	**F**ocused **i**on **b**eam
HRC	**H**ardness after **R**ockwell **C**
HV	**H**ardness after **V**ickers
IBML	**I**on **B**eam **M**aterials **L**aboratory
IVAS	**I**ntegrated **V**isualization and **A**nalysis **S**oftware
LANL	**L**os **A**lamos **N**ational **L**aboratory
LEAP	**L**ocal **e**lectrode **a**tom **p**robe
PKA	**P**rimary **k**nock-on **a**tom
PoSAP	**Po**sition **S**ensitive **A**tom **P**robe (software)
RPV	**R**eactor **p**ressure **v**essel
SEM	**S**canning **e**lectron **m**icroscope
SRIM	The **S**topping and **R**ange of **I**ons in **M**atter (software)
TEM	**T**ransmission **e**lectron **m**icroscope

List of figures

List of tables

1. Introduction

The increasing use of nuclear technology also necessitates the research on materials suitable for nuclear applications. In order to improve the safety, reliability, and efficiency of nuclear facilities or to develop future applications, it is necessary to understand the processes occurring in the material during irradiation. Sample irradiation in reactors or spallation sources is expensive and time-consuming. Proton irradiation has proven to be an effective way to induce radiation defects in the material in a short time and without highly activating it [1]. Although the comparison of the results is not straightforward, ion-beam irradiation has become a popular tool for academic research. Due to the low energy of the protons, the penetration depth is limited. Therefore, small scale testing methods e.g. nanoindentation and micro-compression testing as well as methods for accurate sample fabrication have been developed in recent years [2-4].

During irradiation a large number of point defects are generated in the material, which further evolve into larger defects leading to a change in microstructure, dislocation density, void formation or phase composition. The accumulation of these defects can be delayed or suppressed by providing a large number of defect sinks such as dislocations and interfaces [5].

In this work the maraging steel PH 13-8 Mo was selected due to its outstanding mechanical properties, excellent corrosion resistance and low swelling [6,7]. Moreover, the martensitic matrix and the fine dispersed intermetallic precipitates act as defect sinks, what makes this steel a good candidate for nuclear applications. The influence of irradiation on the precipitation kinetics and changes in the mechanical properties was investigated based on examination of the solution annealed state and an aged condition. The changes in mechanical properties were followed by utilizing nanoindentation and micropillars. The micropillars were produced in a focused ion beam microscope (FIB) and subsequently tested in the nanoindenter using a flat-punch indentation tip. To gain more information about the microstructure atom probe tomography measurements (APT) have been conducted.

2. Theoretical background

2.1. Investigated material

Precipitation hardening has proven to be one of the most effective ways of increasing the strength of a material. The principle of a particle dispersion hindering dislocation movement has then been used in numerous alloying systems and has also led to the development of martensitic hardenable steels, so-called maraging steels. The term “maraging” refers to “martensite” and “aging” and is frequently used for precipitation-hardened Fe-Ni alloys. Due to the precipitation of fine, uniformly dispersed intermetallic precipitates maraging steels combine high strength with an adequate level of ductility.

An addition of 13 at% Cr provides maraging steels with a good resistance for both general and stress corrosion cracking, making them suitable for many applications, such as extrusion dies, injection moulds and nuclear reactor components.

Precipitates develop during a special two-stage heat treatment; namely solution annealing followed by cooling to room temperature and subsequent aging (Figure 1). After the first step of the heat treatment, the structure consists of a soft, but heavily dislocated nickel-martensite with a lattice parameter of a_α=2.878 Å [8]. During the following aging treatment at temperatures between 400 to 600°C small, finely dispersed precipitates emerge [8-10].

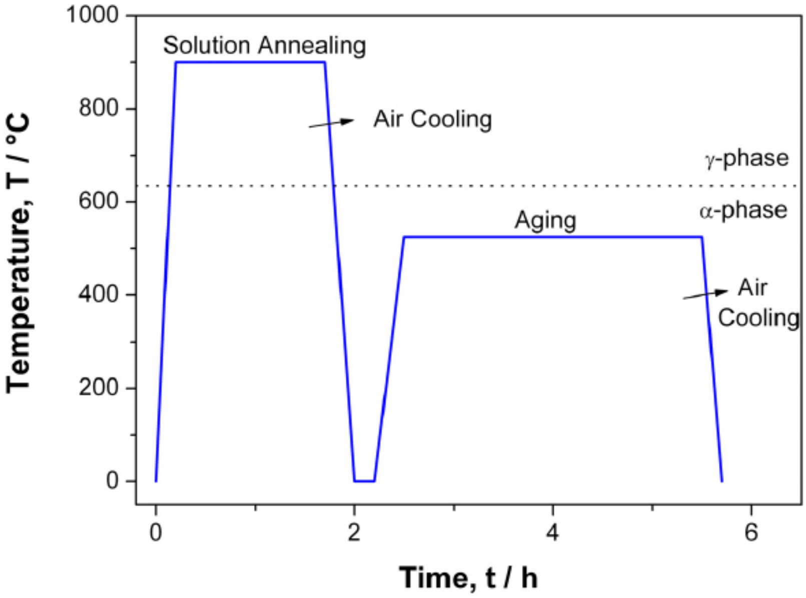

Figure 1. Heat treatment of precipitation-hardened alloys [11].

Most former investigations were carried out on overaged samples due to the inability of resolving the very fine precipitates at the early stages of aging with transmission electron microscopy (TEM). With the advent of atom probe tomography a deeper understanding of the evolution of the precipitates could be gained [12-14].

Guo et al. [12] reported that in PH 13-8 Mo NiAl-enriched zones with a composition far away from the stoichiometric β-NiAl phase are responsible for the increase in strength. The clusters emerge after short time and with persistent aging the amount of Ni and Al in the precipitates increases while the amount of Fe and Cr decreases. The precipitates are randomly distributed in the matrix and it appears that the precipitates emerge through homogeneous nucleation independent of lattice defects such as dislocations [10]. Because the mismatch between the precipitates and the matrix is very low, the precipitates remain coherent even after long durations of aging [8].

Peak hardness is reached after 4 h of aging at 510°C, where the precipitation size accounts for 2-4 nm and their inter-particle distance is several nanometers [14]. With prolonged aging the precipitates experience a classical coarsening process [13] and the chemical composition approaches the equilibrium NiAl-phase which has an ordered B2 (CsCl) superlattice structure [12,14]. Although the size of the precipitates increases with persistent aging, the precipitates are highly resistant to coarsening, allowing the alloy to keep the excellent properties during applications at elevated temperatures [12,13].

The increase in strength due to aging is mainly attributed to NiAl order strengthening and the differences in the shear modulus of matrix and precipitates [8,9]. While [10] related the onset of hardening to the appearance of precipitation, Guo et al. [12] noticed an increase in hardness prior to precipitation which might be due to the redistribution of atoms, i.e. the solute segregation to dislocations.

2.2. Radiation effects in structural materials

Radiation damage in structural materials and consequential changes in mechanical properties are a topic of major concern in designing systems operating in radiation environment. Understanding the processes occurring in the material during irradiation and the changes in microstructure is significant to prevent sudden failure of irradiated parts.

Radiation experiments in reactors are time-consuming, they lead to highly activated samples and they are therefore very costly. Proton irradiation has proven to be a very effective way to emulate the effects of neutron irradiation. Realizing a high dose rate at very short time without activating the sample is one of the substantial advantages of ion-beam irradiation. The main difference is the nature of the displacement cascade and the rate of damage accumulation. In principle, the conditions during proton irradiation can be controlled to arrive at a nearly identical microstructure and microchemistry as in the case of neutron irradiation [1]. Although not all results can be compared directly to neutron experiments, it is a good way to gain basic information about the interaction of radiation and materials.

The radiation damage event is defined as the transfer of energy from incoming ions to lattice atoms in a collision. These lattice atoms are displaced of their original site, also travelling through the lattice displacing more atoms. Hence, each incident ion creates a collision cascade leading to a certain amount of vacancies and interstitial atoms.

The displacement of atoms is the fundamental process that drives the changes in structural materials which leads to a change in their properties [15]:

- Radiation-induced hardening/ embrittlement
  The created point defects can accumulate to voids and dislocation loops or can enhance diffusion, allowing intermetallic precipitates to form. Hindrance of the movement of dislocations by these new obstacles causes radiation-induced hardening and, more important, embrittlement.
- Radiation-induced segregation
  The enhanced diffusion can also result in local segregation around grain boundaries. The enrichment of single elements on grain boundaries and the depletion around it is disadvantageous for the mechanical properties.
- Radiation-induced swelling
  Volume changes and swelling appear due to the formation of voids in the solid, thus, increasing the volume while the density of the material is decreased.
- Radiation-induced creep
  The physical changes also influence the mechanical response of a material when stress is applied. The increased amount of defects can cause phenomena such as radiation-induced creep due to the enhanced ability of the dislocations to overcome obstacles.

In material science the damage due to radiation is measured in the unit displacements per atom (dpa), which means how often one atom has been displaced from its original lattice place.

2.3. Microstructural changes due to irradiation

The long-term stability of structural materials in highly irradiated environments is one of the most important issues affecting the safe and economic operation of nuclear power plants. Since the evolution of the macroscopic properties is related to the evolution of the microstructure, understanding the microstructure evolution under irradiation is essential to predict time-of-life of internals. Thus, since the last decades a large number of studies have focused on the characterization of these microstructural changes under irradiation.

Assuring the structural integrity of the reactor pressure vessel (RPV) is fundamental to the safe operation of nuclear power plants. Therefore, a vast number of studies focused on the degradation of RPV steels under neutron irradiation. Soon it has been recognized that the main mechanism inducing irradiation hardening and embrittlement of these low-alloy steels was connected to the formation of Cu clusters [16]. For better understanding of the formation mechanism of solute clusters in RPV steels, Meslin et al. [17] investigated a low copper and a copper-free model alloy. Solute-enriched clusters have been found in all materials, even in the Cu-free alloy. Clusters mainly enriched in Cu form earlier than clusters enriched in Mn and Ni, leading to the assumption that irradiation induces the Mn and Ni clusters, whereas it accelerates Cu clustering. As materials become more complex, the defects created by irradiation are reduced in size [18]. Hyde et al. [19] studied the differences in cluster formation during heat treatment and irradiation on Cu-containing RPV steels. They found that the chemical composition of the clusters differs according to their origin. More precisely, irradiation-induced clusters have a lower Cu content and higher Mn, Ni and Si contents.

The life-time of austenitic stainless steels in radiation environment is limited by their strength and swelling resistance. Based on an Fe-34.2Ni-5.4Al (wt%) alloy it has been shown [20] that coherent precipitates like Ni_3Al reduce the average concentration of point defects, thereby suppressing the swelling process.

Since ferritic / martensitic steels of higher strength are less sensitive to neutron radiation embrittlement and more resistant to radiation-induced swelling [21], maraging steels containing coherent precipitates appeared to be perfect candidates for materials in radiation environment. Van Renterghem et al. [22] examined an overaged condition of PH 13-8 Mo (560°C for 4 h) using TEM. They found no difference in size, size distribution and density of the precipitates before and after irradiation and concluded that the precipitates are not affected by radiation. They attributed the irradiation hardening described in [23] to the formation of vacancies and interstitials which agglomerate and form dislocation loops, the density and size of which increases with increasing dose. The influence of irradiation at 200°C and 300°C on the mechanical properties on the same condition was investigated by Jong et al. [24]. Among other things they observed that the yield strength hardening and the loss of ductility is larger for the 200°C irradiated sample, implying that at 300°C thermal processes are active, so that the amount of irradiation damage is reduced. The formation development of radiation-induced clusters and the interaction of pre-existing clusters with irradiation are still not fully understood.

2.4. Nanoindentation

2.4.1. Basic principles

Nanoindentation is a technique for measuring hardness and elastic modulus in small-scale. Mechanical properties can be determined directly from indentation load and displacement measurements without the need to image the hardness impression. The advantage of depth-sensing instruments is to keep error and time exposure small as well as the ability to obtain information about elastic and time-dependent plastic properties [2].

Indenters are typically made out of diamond, tungsten carbide, and sapphire and the most common geometries are Vickers (pyramidal with square base), Berkovich (pyramidal with triangular base) and spherical [25]. A Berkovich indenter is more resistant to blunting due to his three-edge construction and has the same area-to-depth ratio as a Vickers indenter which makes the results of nano-tests comparable to micro-tests. Because Vickers hardness uses the area of the residual hardness impression and nanoindentation the contact area, the nanoindentation values need to be multiplied with 0.937 so both types of hardness share the same definition [26].

A typical force versus time cycle for indentation is shown in Figure 2a. After linear loading to the maximum force (a), it is held for a dwell period (b) to allow time-dependent plasticity or creep effects to diminish. Subsequently the specimen is unloaded to 10% of the maximum force (c) and held there for 60 s (d) to measure the thermal drift and then fully unloaded (e) [25].

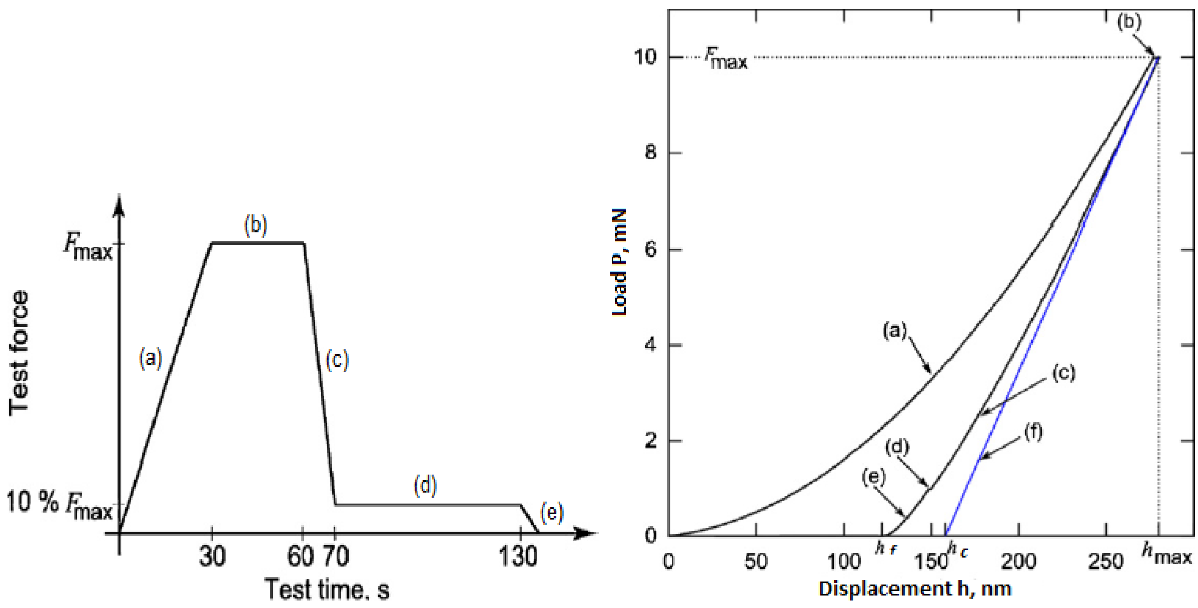

(a) (b)

Figure 2. (a) Typical force vs. time cycle of nanoindentation measurements. (b) Load-displacement data obtain during one cycle of loading and unloading (after [25]).

Load and displacement are continuously detected during the whole cycle leading to a data curve schematically depicted in Figure 2b. During loading elastic and plastic deformation occur, forming the residual hardness impression. It is assumed that only the elastic displacement recovers during unloading and therefore, the unloading curve displays the elastic properties [27].

2.4.2. Data analysis

When load is applied the indenter penetrates the surface to the maximum depth h_{max}. It is assumed that the contact periphery sinks in around the indenter and thus, the contact depth h_c, along which contact is made between the indenter and the sample, is not the maximum depth:

$$h_c = h_{max} - h_s \tag{1}$$

After unloading an impression with the final depth h_f remains as visible mark on the surface. Figure 3 shows a schematic representation of a section through an indentation [27].

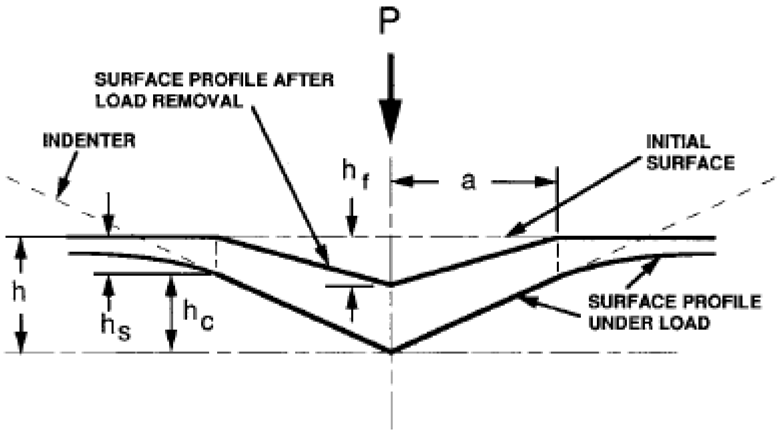

Figure 3. A schematic representation of a section through an indentation showing various quantities used in the analysis [27].

While conventional hardness measurements rely on direct imaging of the residual hardness impression, the error would be enormous using the same technique for nanoindentation. Therefore, the contact area under maximum load is calculated from the indenter shape and the contact depth:

$$A = F(h_c) \tag{2}$$

Awareness of the true contact area leads to the hardness, using the well-known equation:

$$H = \frac{P_{max}}{A(h_c)} \tag{3}$$

The contact depth is not directly amenable in the load displacement curve but can be obtained by means of the contact stiffness *S*, defined as the slope of the unloading curve during the initial stage of unloading (blue line in Figure 2b):

$$h_c = h_{max} - \epsilon \frac{P_{max}}{S} \tag{4}$$

ϵ depends on the indenter shape and is 0.75 for a paraboloid of revolution.

There have been different approaches to measure the contact stiffness, which plays an important role in calculating the true contact area of the indenter and therefore is part of the equation for both hardness and Young's modulus. Oliver and Pharr [27] proposed to approximate the distinct curvature of the unloading curve by the power law relation:

$$P = \alpha(h - h_f)^m, \tag{5}$$

where α and m are power law fitting constants and h_f is the final depth. The initial unloading slope is then found by analytically differentiating this expression and evaluating the derivative at peak load and displacement:

$$S = \frac{dP}{dh} \tag{6}$$

The reduced elastic modulus E_{eff}, which takes into account that elastic displacement does not only occur in the specimen but also in the indenter, follows from its relationship to contact area and measured unloading stiffness:

$$S = \frac{2}{\sqrt{\pi}} E_{eff} \sqrt{A} \tag{7}$$

With the knowledge of Young's modulus E_i and Poisson's ratio ν_i of the indenter, the elastic constants of the specimen can be calculated:

$$\frac{1}{E_{eff}} = \frac{1-\nu^2}{E} + \frac{1-{\nu_i}^2}{E_i} \tag{8}$$

The Oliver and Pharr method [27] has established as standard method and will be used in all analyses of this work.

2.4.3. Corrections

To obtain reproducible results independent from environment and set-up some corrections need to be applied.

- For materials with distinctive time-dependent behavior the dwell period needs to be elongated to allow creep effects to diminish.
- It is best to wait until thermal equilibrium in the indentation chamber is established. Further changes in indentation depth from thermal expansion or contraction of the sample can be measured at a constant force and corrected afterwards [28].
- During indentation the observed indentation depth is a combination of sample penetration and bending of the frame. The frame compliance is a constant value for small forces, but is load-dependent for higher forces:

  $$h' = h - C_f P \tag{9}$$

  From the measured depth h the frame compliance C_f under the load P has to be subtracted to receive the corrected depth h' [28].

- Forming a hardness impression is associated with the movement of material. Depending on the ratio of the effective modulus to the yield stress, E_{eff}/σ_y, and the work-hardening behavior pile-ups may occur. Pile-ups result in an overestimation of the contact area, leading to similar errors in the hardness, and the modulus will be in error by a factor that scales as $\sqrt{A}$. Atomic force microscope examinations have to be conducted to measure the amount of pile-up [2].
- Another big influence on the obtained contact area is the indenter shape. In practice, it is not possible to manufacture a perfectly sharp indenter tip. Moreover with proceeding use the indenter blunts, distorting the contact depth h_c, and therefore, the contact area (Figure 4).

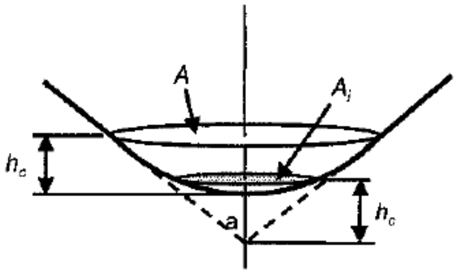

Figure 4. Indenter tip blunting results in a distorted contact depth h_c and therefore an error in the contact area [28].

  This error can be corrected by applying an area correction function which is obtained by performing indentations on a reference sample. The correction becomes less important with increasing indentation depth [28].

- The indentation size effect is a well-known phenomenon whereby the measured hardness values increase with decreasing load. De Guzman et al. [29] explained that behavior by the concept of geometrically necessary dislocations, which are the dislocations forming the residual hardness impression. At shallow penetration depths the density of dislocations underneath the indenter tip is very high yielding to a higher hardness value. This effect diminishes with increasing penetration depth and the hardness approaches the intrinsic value.

2.5. Atom probe tomography

The atom probe is a microscope that provides chemical information on the analyzed volume with near atomic resolution in three dimensions and is therefore very suitable for the examination of the early stages of precipitation. It is a further development of a field ion microscope (FIM) where field ionization is used to image the surface of a needle-shape specimen. Into the ultra-high vacuum test chamber (<2*10^{-8} Pa) a trace of an image gas, typically 10^{-3} Pa of neon or helium, are introduced. When positive voltage is applied to a cryogenically-cooled specimen tip, near-by image gas ions are field ionized and repelled from the surface towards a phosphor screen. As the ionization rate is highest over the most protruding surface atoms, the field ion image shows the positions of these atoms [30].

An atom probe uses the same principle, but the electrical field is further increased by pulsing the voltage up from a standing voltage and ions are consequentially field evaporated. Additionally, atom probes contain a time-of-flight mass spectrometer and a position-sensitive single atom detector, allowing a three-dimensional reconstruction of the investigated material. The latest generation of atom probes is featured with a local electrode [31], as shown in Figure 5. The major benefits of the local electrode are an increase in the field of view and a lower-amplitude standing and pulse voltage, allowing higher pulse repetition rates and therefore reducing the acquisition time. Moreover, the possibility of localizing the evaporation field within a small region allows the use of multi-tip arrays.

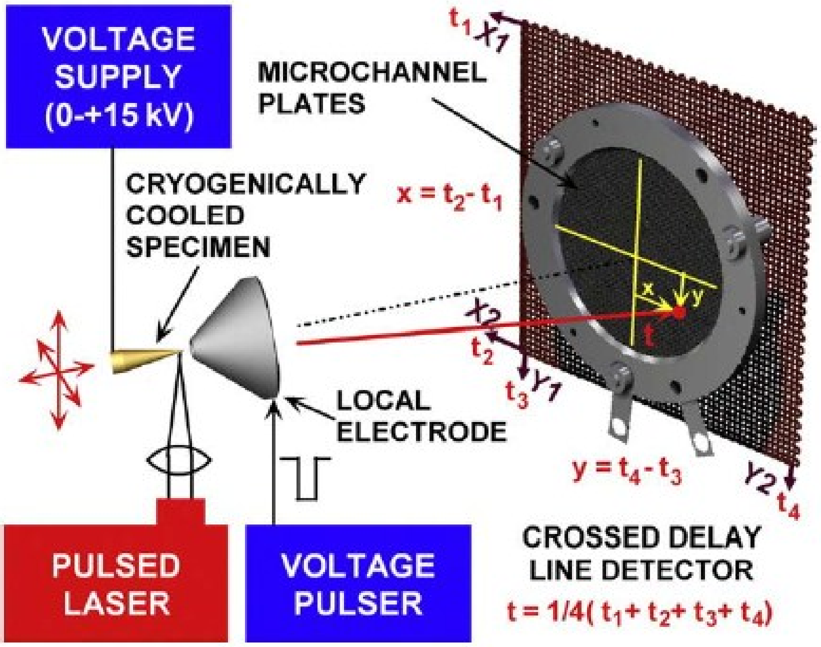

Figure 5. Schematic diagram of a local electrode atom probe (LEAP) [32].

As the detector position can be related to the initial position of the atom on the needle apex assuming a simple projection law and the sequence of evaporation is used to provide depth information, the evaporated material can be reconstructed in three dimensions. The chemical identification of the single atoms follows based on the mass-to-charge ratio $\frac{m}{n}$:

$$\frac{m}{n} = \frac{c(V_{dc}+\alpha V_{pulse})t^2}{d^2} \qquad (10)$$

C is a constant (c=1.93x10^{-4}) used to convert mass into atomic mass units, V_{dc} and V_{pulse} are standing and pulse voltage, α is the pulse amplitude coupling factor which accounts for some loss in the effectiveness of the pulse, d is the distance between specimen apex and detector and t is the time of flight, which results from the time between the evaporating pulse and the atom detection. The typical detection efficiency is 50-60% of the removed ions, but due to fact that it is the same for all elements a truthful reflection of the chemical composition is ensured [32].

A typical use of atom probe tomography is to visualize nanometer-sized precipitates and determine their size, shape, composition, number density and volume fraction. Software packages such as PoSAP or IVAS from Cameca Science of Metrology Solutions offer a wide range of analyzing tools. Tools applied in this thesis, e.g. frequency distribution, radial distribution function and the cluster search algorithm, will be explained in more detail based on the obtained data.

3. Experimental

3.1 Specimen preparation for the irradiation

The investigated PH 13-8 Mo was commercially produced and provided by the company Böhler-Uddeholm. The nominal chemical composition is given in Table 1. The alloy was delivered in the solution annealed condition (850°C, 0.5 h). Subsequently, part of the material was aged at 500°C for 2 h.

Table 1. Typical chemical composition of PH 13-8 Mo in wt% according to the data sheet of 2010 [33].

	Fe	C	Cr	Ni	Al	Mo	Mn	Si
PH 13-8 Mo	Bal.	0.03	12	9.2	1.6	1.4	0.3	0.3

Pieces of 20 mm x 20 mm x 10 mm of the solution annealed and the aged condition were grinded with Silicon metallurgical paper up to 1200 grit and polished with diamond suspension with a particle size of 3 and 1 µm at a Struers Rotopol-V. As the last step the samples were polished with 0.1 µm colloidal silica suspension for approximately 3 h on a Buehler VibroMet 2 polisher.

3.2. Calculation of parameters for the irradiation with SRIM 2008

The goal of the irradiation was to create a damage of 2 dpa. The resulting damage profiles and the beam parameters can be calculated by Monte Carlo methods, for example the SRIM (The Stopping and Range of Ions in Matter) code version 2008.04 [34]. Necessary parameters for the calculation are:

- Type and energy of the incident particles
- Composition and density of the target material
- Displacement energy
- Beam current
- Size of the irradiated area

The radiation experiments were performed at the Ion Beam Material Laboratory (IBML) at the Los Alamos National Laboratory (LANL) using a 3.2 MV tandem ion accelerator. The accelerated ions, in this case ionized hydrogen, hit the target with an energy of 1.3 MeV. The energy of the ions and the composition of the target

(Table 1) determine penetration depth and extension of the radiation damaged zone. The incident ion impinges on a target atom, transfers parts of its kinetic energy and as a result the struck atom, also called a primary knock-on atom (PKA), is displaced of its original lattice site. The ion and the PKA travel through the lattice, creating additional knock-on atoms what leads to a displacement cascade. Kinchin and Pease [35] developed a model to calculate the amount of vacancies created by a PKA depending on its energy *T*. The result of their model is shown in Figure 6, where E_d is the displacement energy, the minimum energy a lattice atom must receive in a collision to be displaced from its site, and E_c is a cut-off energy above which no additional displacements occur until the PKA energy decreased to it.

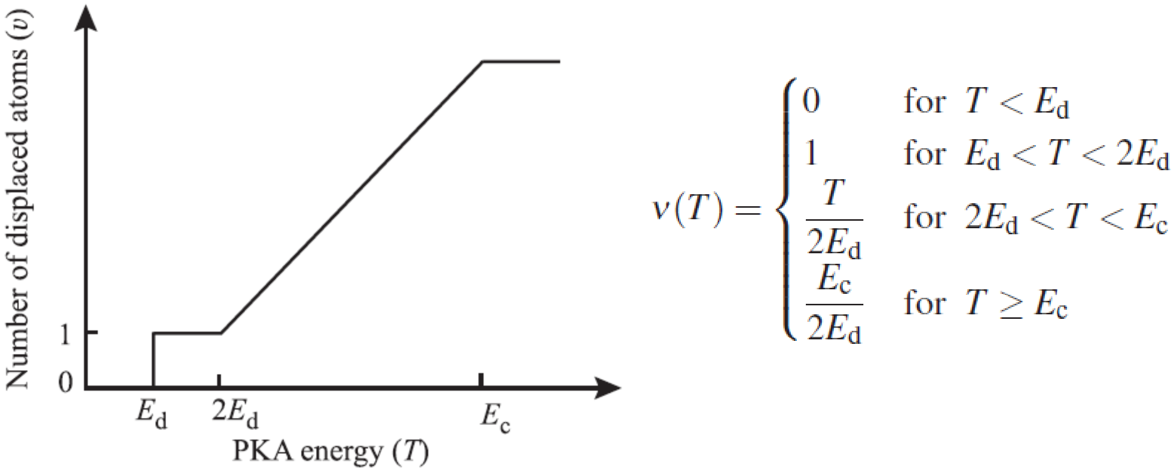

$$\nu(T) = \begin{cases} 0 & \text{for } T < E_d \\ 1 & \text{for } E_d < T < 2E_d \\ \dfrac{T}{2E_d} & \text{for } 2E_d < T < E_c \\ \dfrac{E_c}{2E_d} & \text{for } T \geq E_c \end{cases}$$

Figure 6. The number of displaced atoms in a cascade as a function of the PKA energy according to the model of Kinchin and Pease [15].

The displacement energy arises from the potential fields around the struck atom, which the atom has to pass in order to be displaced. The potential barrier is not equal in all direction. For simplification a single value, which represents a spherical average of the potential barrier surrounding the equilibrium lattice site, of 25 eV is given for the displacement energy [15]. With this information the SRIM code calculates the damage rate *D*, the produced vacancies per incoming ion per angstrom:

$$D = \frac{vac}{ion * \text{Å}} \tag{11}$$

To get the damage in displacements per atom, the calculated damage profile was multiplied with the current density *j*, and the reciprocal of the atom density *ρ:*

$$D * j * \frac{1}{\rho} = dpa \tag{12}$$

The current density can be determined by measuring the current induced in the sample and the time the sample is exposed to the beam:

$$j = \frac{I}{A * t} \tag{13}$$

where *I* is the beam current, *A* the irradiated area on the sample and *t* the irradiation time. During irradiation the beam current was logged and the exposure time was adapted according to the desired dose. Table 2 summarizes the irradiation parameters.

Table 2. Parameters of the irradiation experiment.

Ion	Energy [keV]	Temperature [°C]	Current [µA]	Area [mm^2]	Time [h]	Depth [µm]	Dose [dpa]
H^+	1300	RT	~2.5	2.5x2	20	~10	2

3.3. Sample irradiation

The radiation experiments were performed at the Ion Beam Material Laboratory (IBML) at the Los Alamos National Laboratory (LANL) using a 3.2 MV tandem ion accelerator. A schematic diagram of the set-up and an image of the accelerator are depicted in Figure 7 and Figure 8a. The ions extracted from the ion source have an energy of 50 keV. A tandem accelerator consists of two accelerating tubes which are connected by a high voltage terminal. At the terminal a high positive voltage is applied accelerating the negative ions towards it. The ions pass through an electron stripper where the negative ions are converted into positive ones which are repelled by the terminal. At each step the ions were accelerated by 0.647 MeV, leading to a total energy of 1.344 MeV [36].

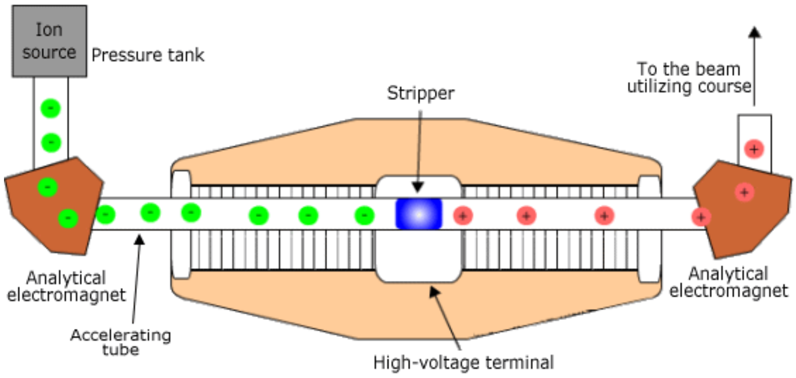

Figure 7. Schematic diagram of a tandem accelerator (after [37]).

Two samples at a time were mounted on a copper sample holder, shown in Figure 8b, using silver paste and carbon tape to ensure good adhesion and thermal conductivity to dissipate the induced heat. During the experiment the temperature was measured with a thermocouple which was located underneath the sample and the current induced in the sample was monitored.

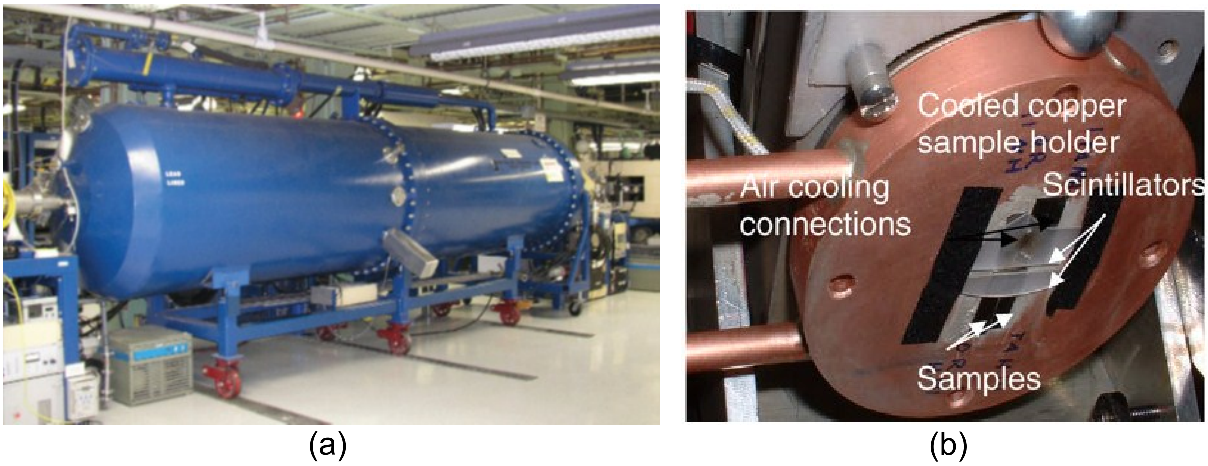

Figure 8. (a) Tandem ion accelerator at IBML in LANL [36]. (b) Sample mounting in the ion beam irradiation experiment [38].

Figure 9 shows the calculated damage profile in dpa. The blue curve represents the amount of vacancies created in the material; the red curve illustrates the stopping range of the Hydrogen ions. The damage is nearly uniform through the first 8 µm of the total range of 10 µm, resulting in a damage of 2 dpa.

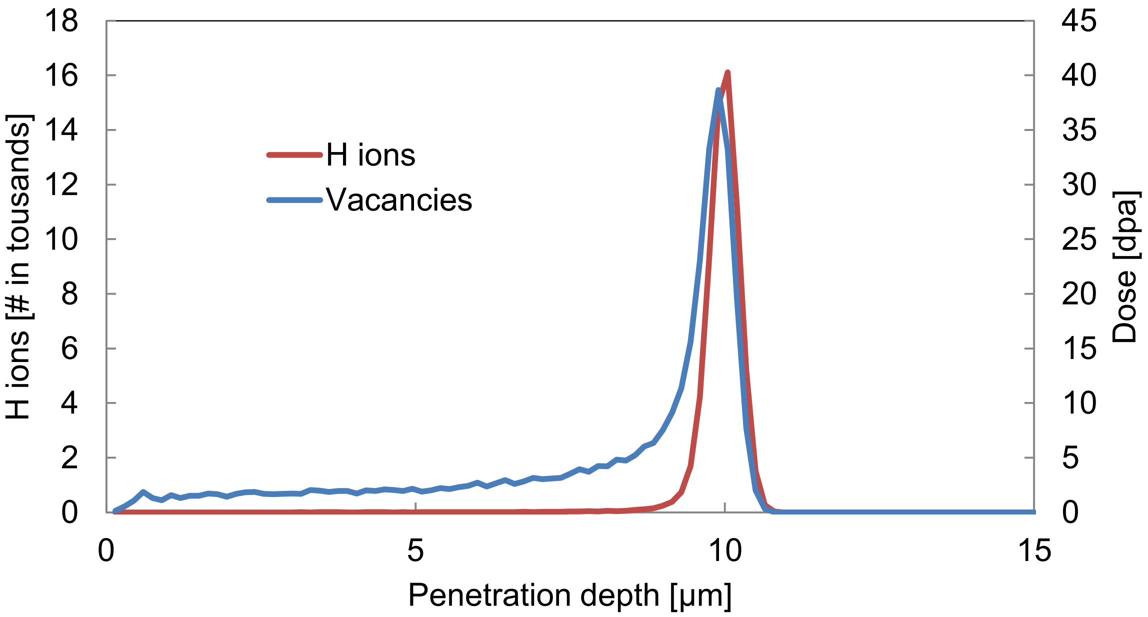

Figure 9. Damage profile over penetration depth calculated using SRIM 2008.

3.4. Nanoindentation

After the irradiation the samples were embedded upright in epoxy cold mount to investigate the cross section. As the last step of the preparation the samples were polished with 0.1 µm colloidal silica on a Buehler vibromet polisher.

The nanoindentation measurements were conducted at UC Berkeley, California, USA, on Micro Materials NanoTest^{TM}, schematically shown in Figure 10. The vertically system is based on a pendulum that can rotate on a friction-less pivot. On top of the pendulum a coil and a magnet are mounted. When current is applied the coil is attracted to the magnet and the indenter tip penetrates the surface of the specimen electromagnetically. The imposed force is controlled by varying the current in the coil. The indention depth is measured by means of a capacitor; one plate is attached to the diamond hold, changing therefore the capacity according to the depth of indentation [39].

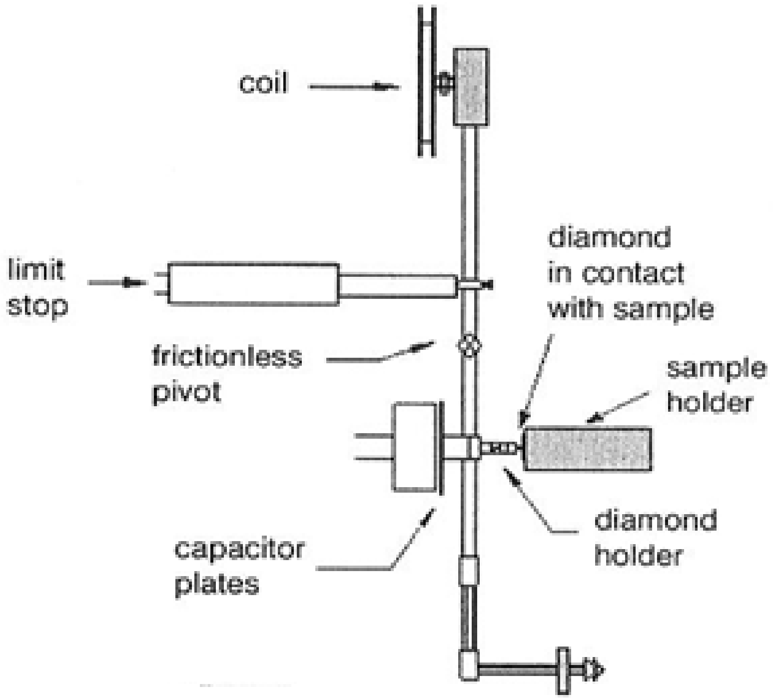

Figure 10. Schematic diagram of Micro Materials NanoTest^{TM} [39].

A Berkovich diamond indenter tip was used to perform the nanoindentation measurements. Constant displacement mode was applied for all indentations on the cross-section to ensure constant indentation depth. Moreover, it eliminates the influence of the indentation size effect in one array of indentations. Starting from the edge 5 rows with 20 indentations to a nominal depth of 200 nm were conducted. The rows were set in an angle of about 20° for better resolution. The indentations were 4 µm apart from each other, resulting in a grid of 100 indentations measuring as far as 25 µm away from the edge, as shown in Figure 11.

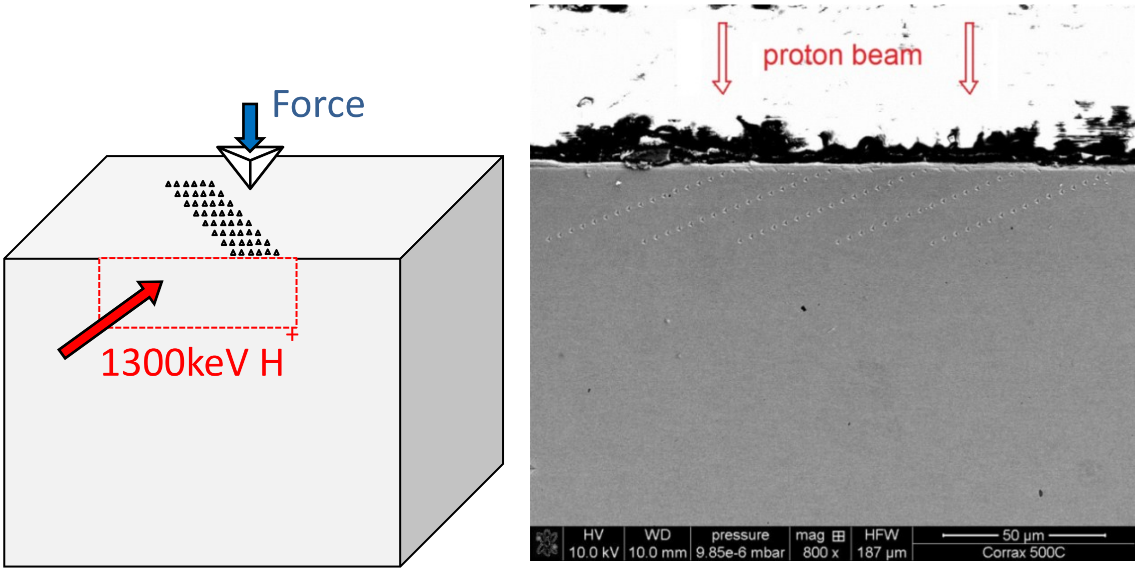

(a) (b)

Figure 11. (a) Schematic sketch of the nanoindentation measurements. (b) A scanning electron micrograph of one array of indentations on the cross section of the sample aged for 2 h at 500°C.

3.5. Atom probe tomography

The ATP measurements were conducted at the Center for Advanced Energy Studies (CAES) in Idaho Falls, ID, USA. For all measurements a LEAP 4000X HR was used.

Usually needle-shaped specimens are fabricated by a standard two-step etching method [40]. Since in this case material of a specific location was needed a FIB-based lift-out method was applied [4,41,42], as shown in Figure 12. First a protective platinum layer was deposited on top of the region of interest. Then two rectangular cross sections were trenched at a distance of about 2 µm above and beyond the region of interest to receive a blank of 25 µm x 2 µm x 15 µm. The specimen was tilted 52° with respect to the ion beam to perform the undercut. Before the final side was cut free the blank was attached to the lift-out probe through platinum deposition. The blank remained on the lift-out probe while the bulk specimen was replaced by a multi-tip array. The end of the blank was attached with platinum deposit to a post on the array and subsequently cut free. This process was repeated with the rest of the material. Subsequently, needle shaped samples with a circular cross-section, an end radius of about 50 nm, and a taper-angle below 5° were cut. The last step was a low voltage (2 kV) cleaning step to reduce the ion beam influenced region.

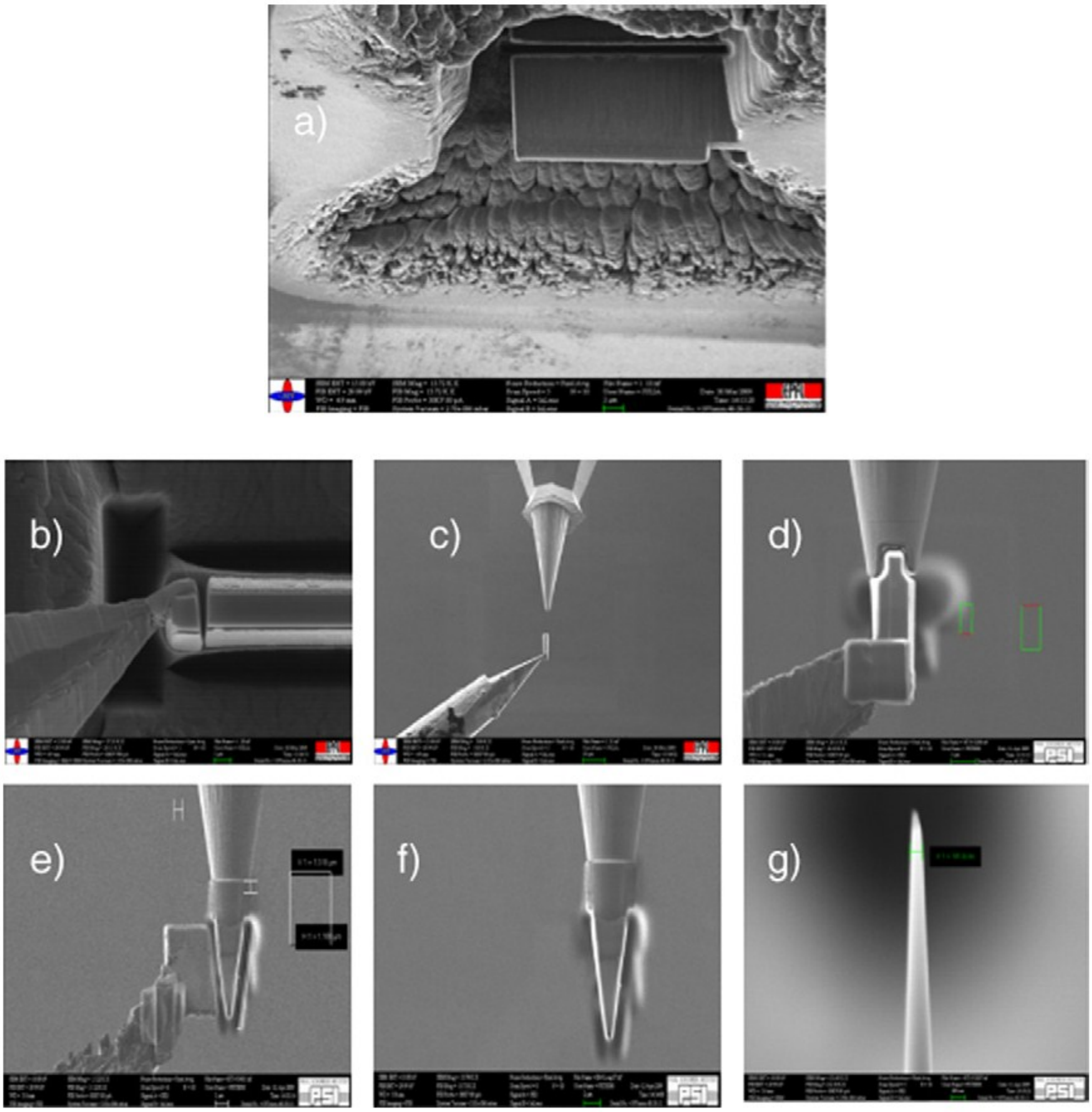

Figure 12. FIB-based manufacturing of an atom probe needle. (a) Fabrication of a blank of 25 µm x 2 µm x 15 µm. (b) - (d) Cutting one strip of the foil and welding it to a sample stub on the multi-tip array. (e) – (f) Alternatively the entire foil can be transported to the multi-tip array and then cut into pieces. (g) The final sharp needle [43].

The atom probe experiments were performed at a temperature of ~65 K in an ultrahigh vacuum (10^{-9} Pa) using a pulse fraction of 20% of the standing voltage. Data reconstruction and statistical evaluation were conducted using the software package IVAS^{TM} 3.6.0 from Cameca Science and Metrology Solutions.

3.6. Micro-compression testing

Uniaxial compression tests were performed on the solution annealed sample on the irradiated and the unirradiated area. The main benefit of micro-compression testing compared to nanoindentation is that no strain gradient is imposed. The pillars were machined with a FEI Quanta4000 FEG dual-beam focused ion microscope using Ga^+ ions with a kinetic energy of 30 keV. Rough cuts were performed at a current of 15 nA at an angle of 52°. It is necessary to mill an area large enough so that the flat-punch indentation tip of a diameter of 30 µm does not hit any surrounding material. Subsequently, the pillars were shaped at an angle of 54° to mill away the visible taper of the sidewalls using a lower beam current (0.5-3 nA) to minimize re-deposition [3]. The pillars in the irradiated zone were placed close to the edge to make sure the whole volume of the pillar suffered radiation damage.

The uniaxial compression experiments were performed at UC Berkeley, California, USA, on MicroMaterials NanoTest^{TM} outfitted with a diamond flat-punch indentation tip. It is challenging to mount the flat-punch perpendicular to the sample surface and therefore ensure proper contact at the initial stage of the experiment. Contact misfit leads to smearing the transition from elastic-to-plastic flow as well as a lower measured modulus upon initial loading. As proposed by Uchic and Dimiduk [3] a custom sample holder containing a miniature goniometer was used for sample alignment, shown in Figure 13.

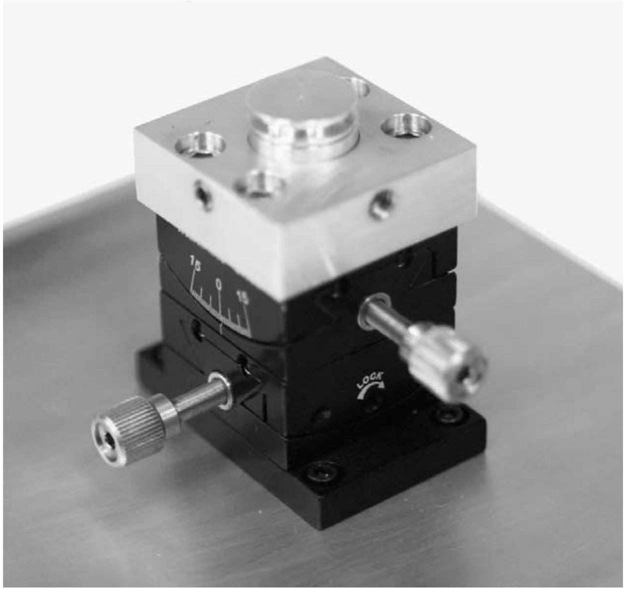

Figure 13. Custom sample holder containing a miniature goniometer to ensure proper sample alignment [3].

The pillars were tested with a loading and unloading rate of 1 mN/sec using load-controlled mode.

The frame compliance, c_f=0.41464866, was applied according to [28]:

$$h' = h - c_f * P \tag{14}$$

where *P* is the load, *h* the measured depth and *h'* the corrected depth.

It needs to be considered that compression not only occurs in the pillar but as well in the underlying material. Sneddon [44] analytically solved the problem of pushing a rigid punch into an infinite half-space. Supposing that the behavior of the underlying material can be approximated with this relationship, the column displacement can be calculated as suggested by Volkert and Lilleodden [45]:

$$\Delta h = h' - \frac{(1-v^2)}{E} * \frac{P}{\frac{d_1+d_2}{2}} \tag{15}$$

E is the Young's modulus and *v* is the Poisson's ratio of the underlying material. D_1 and d_2 are the dimensions of the pillars gained in the scanning electron microscope (SEM) mode of the dual-beam FIB.

The obtained load-displacement curves were transformed into engineering stress-strain curves by

$$\sigma = \frac{P}{(d_1 * d_2)} \tag{16}$$

and

$$\epsilon = \frac{\Delta h}{h} \tag{17}$$

The dimensions of the pillars were obtained in the SEM mode of the dual-beam FIB prior to testing. *h* is the column height, defined as the vertical distance between the extrapolated intersections of the inclined walls and the top of the column.

4. Results

4.2. Optical microscopy

All heat treated conditions were examined through optical microscopy in order to ensure the absence of detrimental phases such as δ-ferrite, which deteriorates mechanical properties and corrosion resistance [46]. As recommended in [47] the samples were etched with “Calling 1” which contains Cu_2Cl and HCl as key constituents. As expected, both samples appear to be fully martensitic, as shown in Figure 14. However, it is know from [48] that PH 13-8 Mo has a phase fraction of austenite of 2.4 vol% after solution annealing and 4.6 vol% after aging for 0.25 h at 525°C. From this can be derived that both conditions examined here could contain a small amount of austenite which is advantageous for the toughness [49]. However, it has not been confirmed by X-ray diffraction measurements.

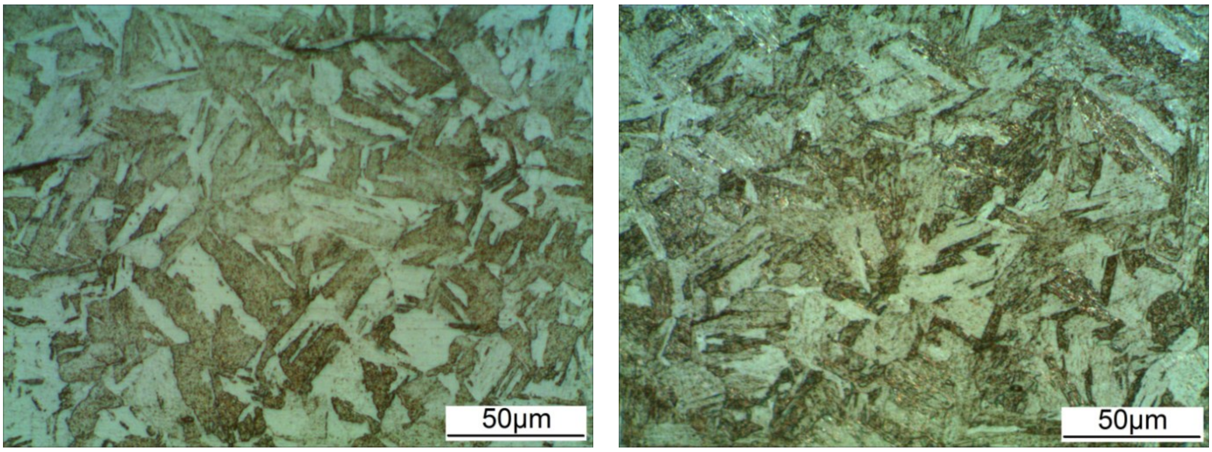

(a) (b)

Figure 14. Optical micrographs of (a) the solution annealed condition and (b) after aging for 2 h at 500°C.

4.3. Nanoindentation

Figure 15 illustrates one line of indentations on the solution annealed sample taken in the SEM mode of the dual-beam FIB. The obtained hardness values are shown in Figure 16. The blue curve illustrates the calculated damage profile and the red points represent the hardness values from nanoindentation. The low hardness values for the indentations close to the edge result from the extent of the plastic zone into the softer epoxy cold mount. In the irradiated area the hardness is about 6.7 GPa, compared to a hardness of about 5.6 GPa in the not irradiated material showing a significant hardness increase due to irradiation. The irradiated / unirradiated interface can be accurately measured using nanoindentation and agrees well with SRIM calculations. Also the stopping peak, where the material suffered a much higher damage and therefore the hardness increase is higher as well, is clearly detectable.

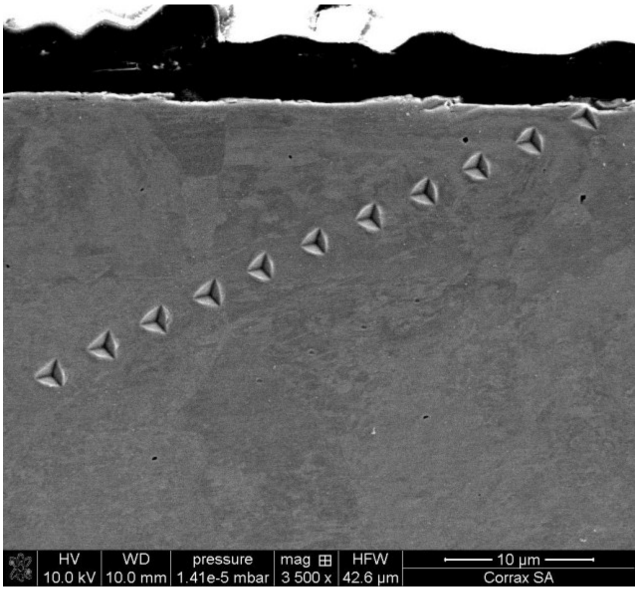

Figure 15. One line of indentations on the solution annealed sample.

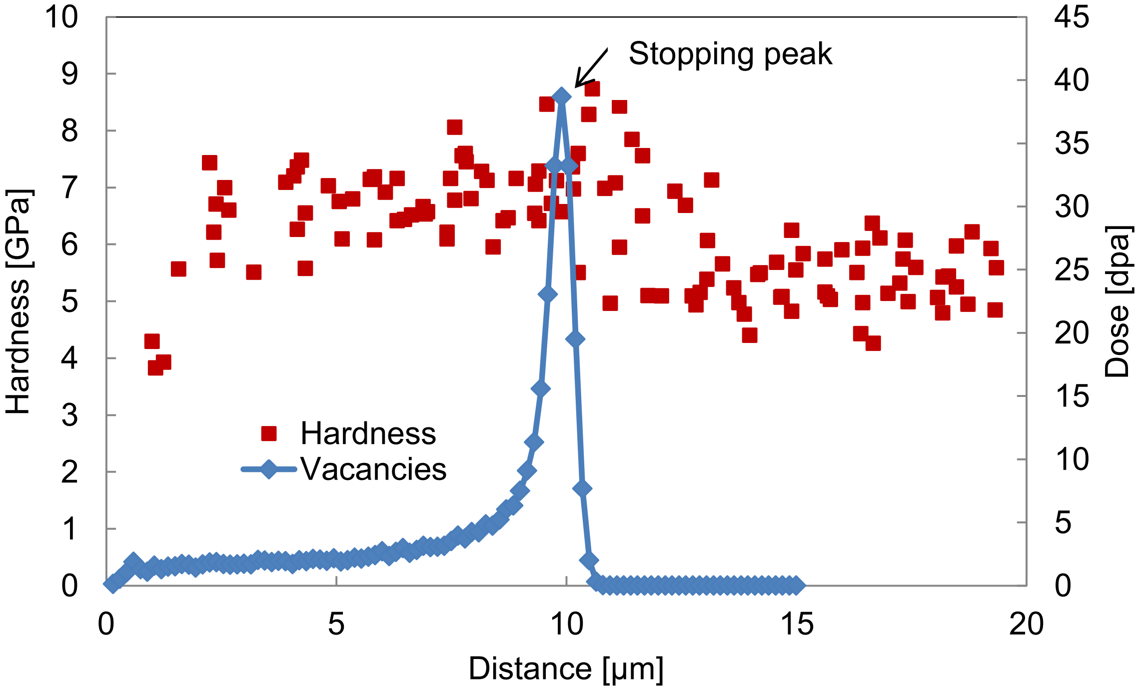

Figure 16. Hardness measured with nanoindentation and the calculated damage profile over the distance from the edge.

Figure 17 depicts the hardness profile measured on the sample aged for 2 h at 500°C. The hardness of the aged material is much higher compared to the solution annealed state. This is due to precipitation hardening during aging compared to the solution annealed state. Irradiation only causes a very small increase in hardness of about 0.4 GPa from 6.7 GPa in the not irradiated area to 7.1 GPa in the irradiated area.

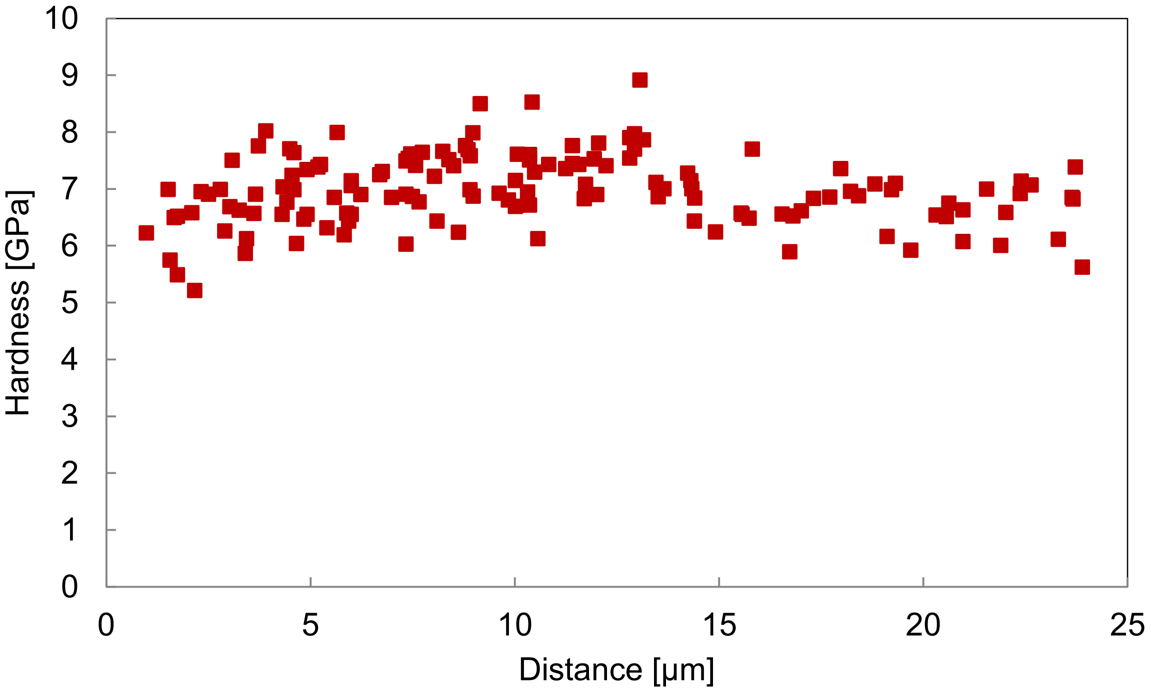

Figure 17. Hardness profile over the distance from the edge on the aged sample.

The obtained hardness values are compared to the nominal hardness values of the data sheet from Böhler Uddeholm [33]. By applying the equations:

$$HRC \sim 116 - \frac{1500}{\sqrt{HV}} \tag{18}$$

and

$$HV = H_{Berkovich} * 0.937 \tag{19}$$

the nominal hardness values are converted from hardness after Rockwell (HRC) into hardness values expected with Vickers (HV) or Berkovich indenter tips [26]. These values are compared to the experimental results gained by macro Vickers hardness tests and nanoindentation. As can be seen in Table 3, Vickers results match quite well, whereas the Berkovich hardness values measured with the nanoindenter exceed the expected values. The hardness in the not irradiated area of the solution annealed sample is 5.6 GPa, compared to a calculated value of 3.5 GPa. Likewise, the measured hardness of 6.7 GPa on the aged sample exceeds the calculated hardness of 5.5 GPa. This can be attributed to the indentation size effect, whereupon the hardness increases with decreasing load. It is also interesting to notice that the difference is smaller on the aged sample because the indentation size effect is less pronounced due to the higher intrinsic hardness.

Table 3. Comparison of the hardness of the solution annealed and the aged condition according to the data sheet of 2010 [33], calculations and experiments.

Samples	Corrax data sheet	Calculated		Measured		
	Rockwell [HRC]	Vickers [kp/mm^2]	Berkovich [GPa]	Vickers [kp/mm^2]	Berkovich [GPa]	
					not irr.	irr.
SA	34	325	3.5	336	5.6	6.7
500°C	50	500	5.5	520	6.7	7.1

4.4. Atom probe tomography

4.4.1. Solution annealed condition

Atom maps of Fe, Cr, Ni, Al and Si of the solution annealed state are depicted in Figure 18. Through optical inspection of the three-dimensional reconstructions random distribution of all elements can be found. This impression is confirmed by a frequency distribution (FD) analysis. If all atoms of one type of element are of random distribution the frequency distribution follows a binomial model [32]. A significant deviation of the binomial model indicates a non-random arrangement of the element.

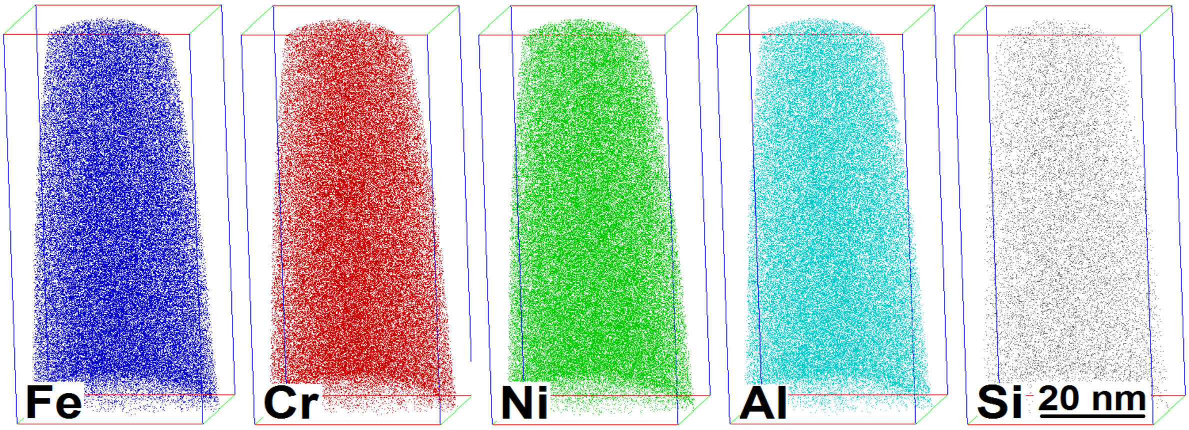

Figure 18. Atom maps of Fe, Cr, Ni, Al and Si of the solution annealed state. There are no segregations visible.

4.4.2. Solution annealed and irradiated condition

ATP measurements were also performed on the solution annealed condition after irradiation to get more knowledge regarding the effect of irradiation on the microstructure. The distribution of the elements seems to be homogeneous from visual inspection of the atom maps of Fe, Cr, Ni, Al and Si, shown in Figure 19. However, FD analysis results provided in Figure 20 reveal that all main elements are not randomly distributed. When phase separation occurs, the experimental concentration distribution deviates from the binomial distribution. The deviation of the observed distribution from the binomial can be quantified by means of Chi-square statistics [50]:

$$X^2 = \sum_{n=0}^{n_b} \frac{(e(n)-f(n))^2}{f(n)} \qquad (20)$$

where *e(n)* is the number of blocks containing *n* solute atoms measured experimentally and *f(n)* is the binomial distribution.

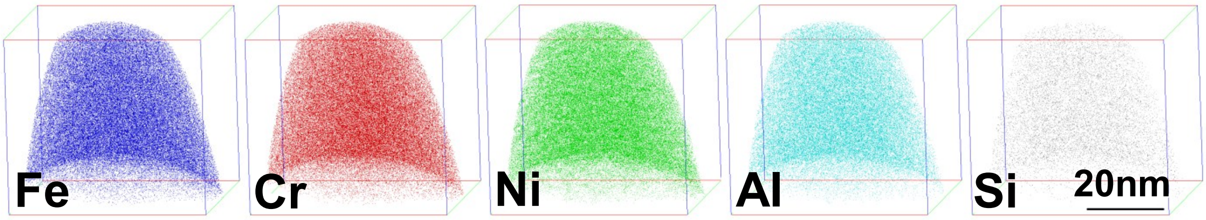

Figure 19. Atom maps of Fe, Cr, Ni, Al and Si of the solution annealed material after 2 dpa proton irradiation.

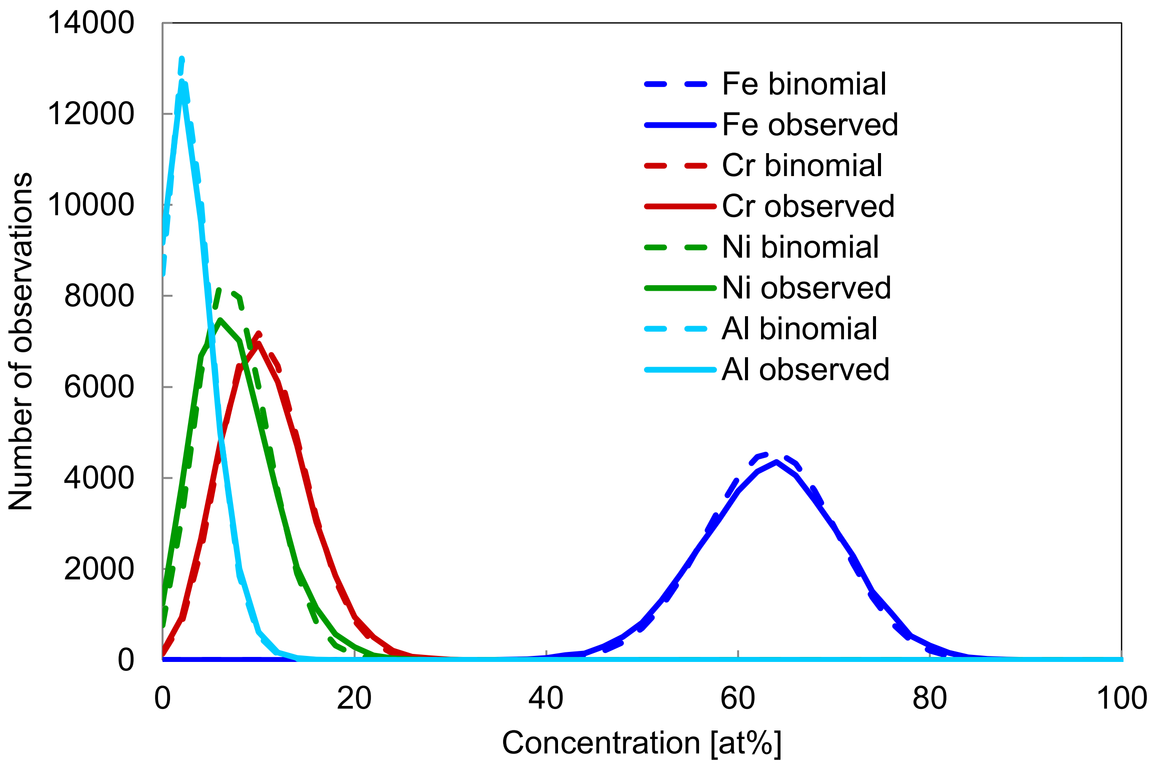

Figure 20. FD analysis of Fe, Cr, Ni and Al of the solution annealed sample. A decomposition of all phases is clearly evident.

To determine whether the differences in the distributions are significant or not, the obtained X^2 values are compared with tabulated values of the Chi-square probability density function. For example, for 4 degrees of freedom the tabulated value of the X^2 probability density function is 18.5 at the 5% level. The calculated X^2 value for Si is 86.4 and thus the probability to make an error when rejecting the null hypothesis that the distribution of Si atoms is random is less than 5%. In the same way the significance of the decomposition of Fe, Cr, Ni and Al is confirmed and the results are presented in Table 4.

Table 4. Results from X^2 statistics of the irradiated solution annealed state.

	X^2	**degrees of freedom**	**theoretical X^2**
Fe	766.1	24	36.4
Cr	247.0	15	25.0
Ni	1717.9	12	21.0
Al	165.0	7	18.5
Si	86.4	4	9.5

Since Ni shows a strong sign of decomposition a radial distribution function, which calculates the concentration as a function of radial distance from all Ni atoms, was calculated. For better visualization the concentration is normalized to the bulk concentration. As can be seen in Figure 21, decomposition mainly enriched in Ni and Si can be detected.

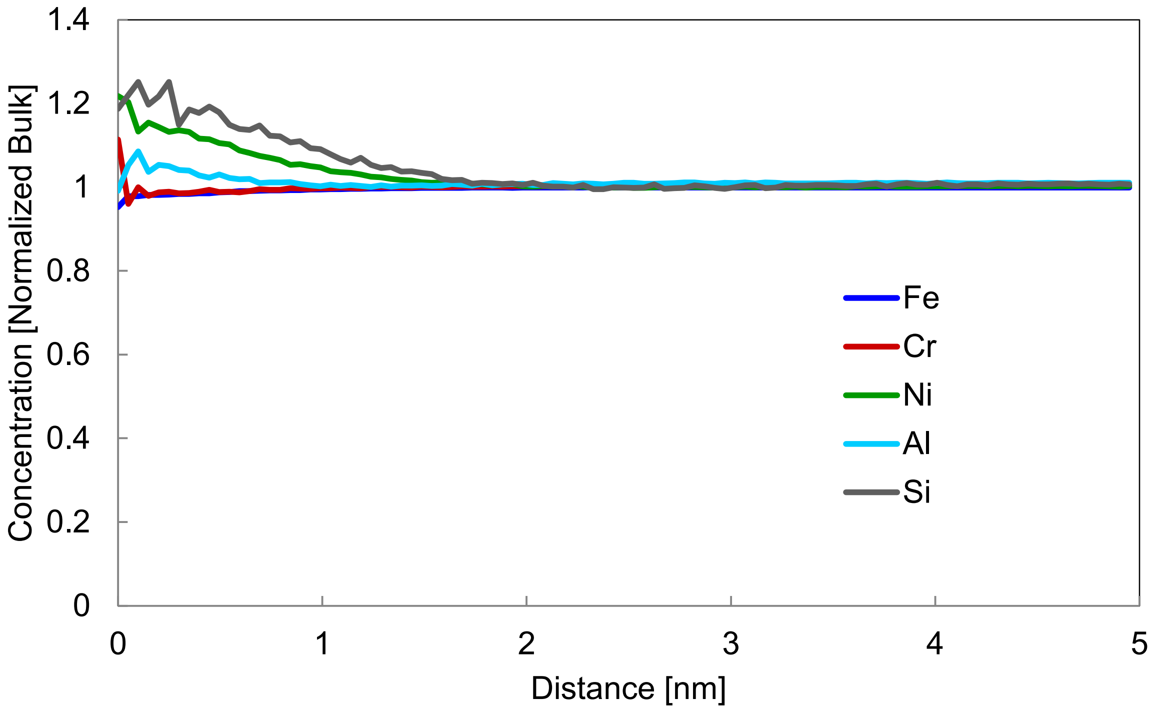

Figure 21. Radial distribution function of Ni of the solution annealed condition after proton irradiation.

4.4.3. Aged condition

Figure 22 shows the analyzed volume after aging the material for 2 h at 500°C. Visual inspection reveals an enrichment of Ni and Al.

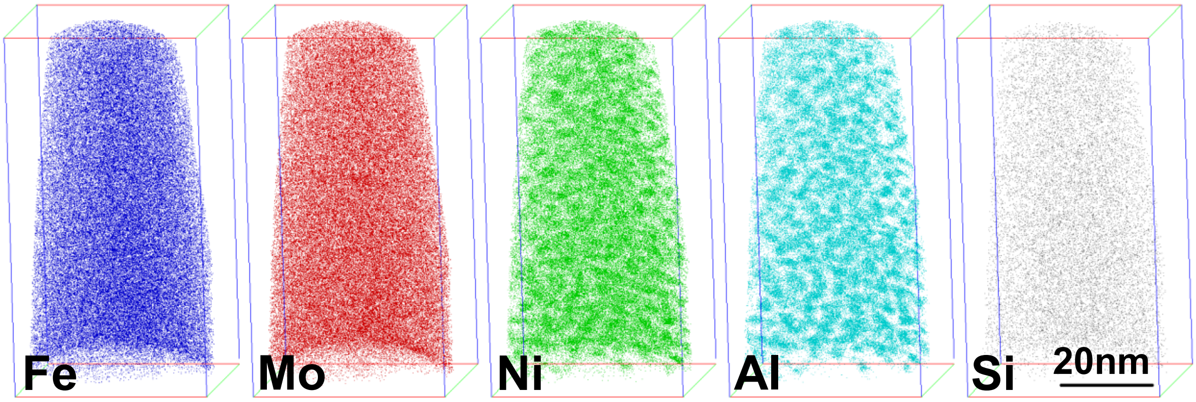

Figure 22. Atom maps of Fe, Cr, Ni, Al and Si of the material after aging for 2 h at 500°C.

A very useful tool to define solute-rich regions is a cluster search algorithm [51]. In this approach the simulation of a random distribution of atoms is compared to the actual distribution of the solute atoms. Based on that, a distance *d* is selected, which is the maximum distance between two solute atoms, belonging to the same particle. To make sure random accumulations of atoms are not included, a minimum number of solute atoms N_{min} is defined. This number is ascertained by plotting a size distribution for a simulated random distribution and then N_{min} is set to the upper end of the distribution so only non-random clusters are part of the analysis. Once all solute atoms belonging to each particle have been detected, all non-solute atoms lying within a distance *L* around the cluster are also taken to be part of the particle. This last step distorts the composition of the clusters by including matrix atoms at the interface. Therefore, an erosion process to remove the outermost atoms is applied. Using the results of the cluster search, composition, size, shape, number density and volume fraction of the precipitates can be investigated.

For the aged sample *d* and *L* were set to 0.34 nm, the erosion distance was selected to be 0.17 nm and a minimum number of 27 ions was defined. The resulting clusters are illustrated in Figure 23 and the size distribution is depicted in Figure 24. The distribution is similar to a normal distribution and the precipitate sizes range from a radius of 0.4 nm to 1.3 nm. The average radius is 0.73 nm and the number density amounts to $7.5*10^{24}$ m^{-3}.

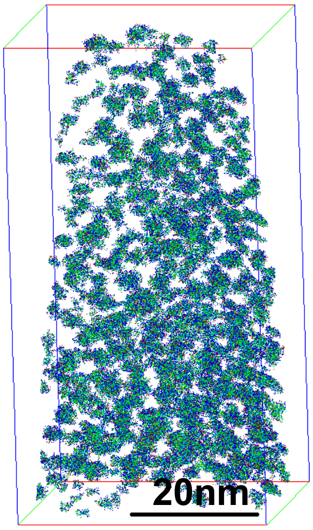

Figure 23. Cluster found by means of the cluster search algorithm in the material after aging for 2 h at 500°C.

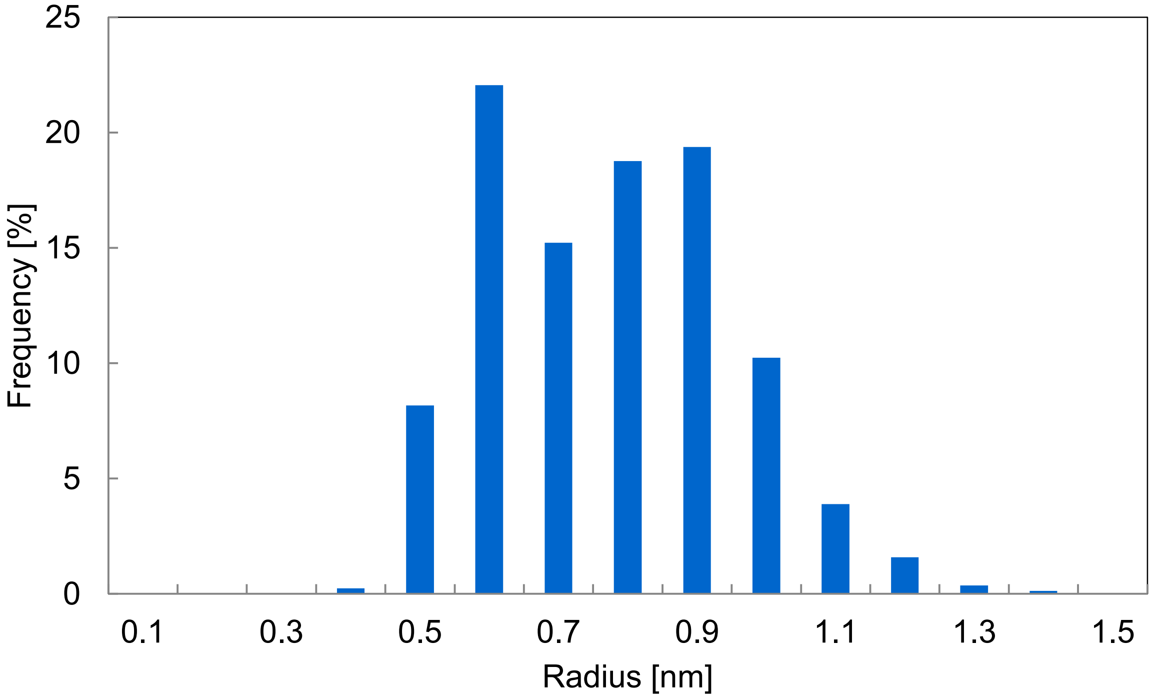

Figure 24. Size distribution of the precipitates after 2 h of aging at 500°C.

Table 5 contains the chemical composition of the precipitates and the matrix based on the cluster search algorithm. The errors on the concentration values are estimated by the standard deviation:

$$\sigma = \sqrt{\frac{c*(1-c)}{N}} \tag{21}$$

where *c* is the measured concentration and *N* the total number of detected atoms. The bulk composition measured with the atom probe matches well with the nominal composition (Table 1). It can be seen that the particles are enriched in Ni, Al and Mn and on the other hand they are depleted of Fe and Cr. Correspondingly, the matrix is depleted of Al and Ni. Nevertheless, the particles contain a high amount of Fe and are still far away from stoichiometric NiAl. For better illustration a radial concentration profile based on the clusters shown in Figure 23 was calculated and depicted in Figure 25.

Table 5. Chemical composition in at% calculated with the cluster search algorithm for the aged sample.

	Fe	Cr	Ni	Al	Mo	Mn	Si	C
Bulk	Bal.	12.27 (±0.02)	8.76 (±0.02)	3.61 (±0.01)	0.76 (±0.01)	0.35 (±0.004)	0.65 (±0.005)	0.05 (±0.001)
Matrix	Bal.	13.04 (±0.02)	6.36 (±0.02)	1.91 (±0.01)	0.87 (±0.03)	0.26 (±0.003)	0.64 (±0.005)	0.06 (±0.001)
Precipitates	Bal.	6.66 (±0.05)	25.97 (±0.10)	15.84 (±0.08)	0.45 (±0.01)	1.02 (±0.02)	0.82 (±0.02)	0.05 (±0.004)

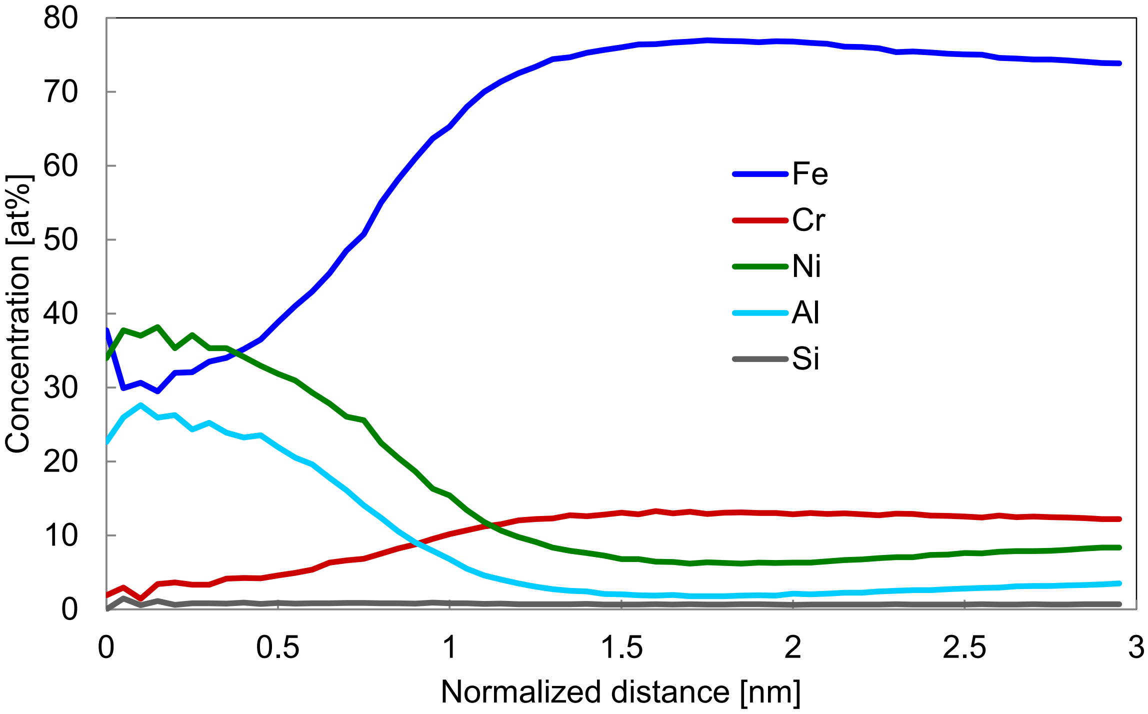

Figure 25. Radial concentration profile of the sample aged for 2h at 500°C based on the clusters shown in Figure 23.

4.4.4. Aged and irradiated condition

Figure 26 illustrates the atom maps of Fe, Cr, Ni, Al and Si of the material after aging for 2 h at 500°C and subsequent proton irradiation to 2 dpa. Again explicit precipitates are discernible.

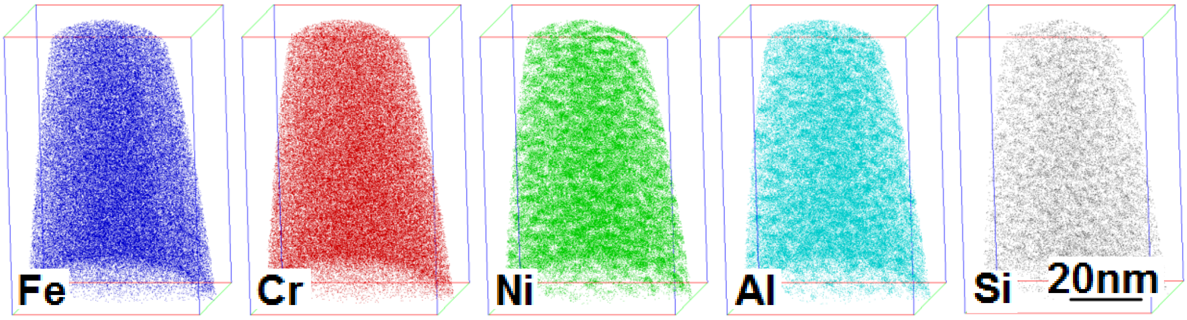

Figure 26. Atom maps of Fe, Cr, Ni, Al and Si after 2 h of aging at 500°C and 2 dpa proton irradiation.

When carrying out the cluster search on the aged and irradiated sample with the parameters *d*=0.34 nm, N_{min}=25, *L*=0.34 nm and l_{eros}=0.17 nm the precipitates as shown in Figure 27 are found.

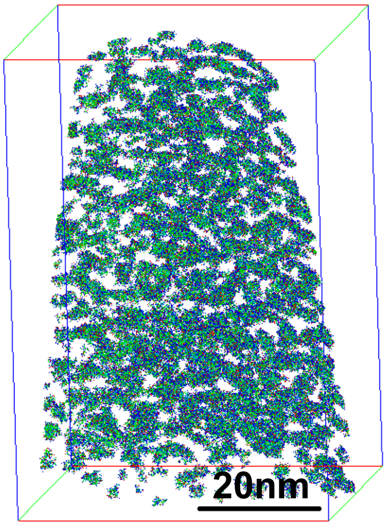

Figure 27. Precipitates in the aged and irradiated sample resulting from the cluster search algorithm.

Figure 28 shows the corresponding size distribution of the precipitates in the aged and irradiated sample. The precipitates have an average radius of 0.72 nm and a number density of 7.6*10^{24} m^{-3}.

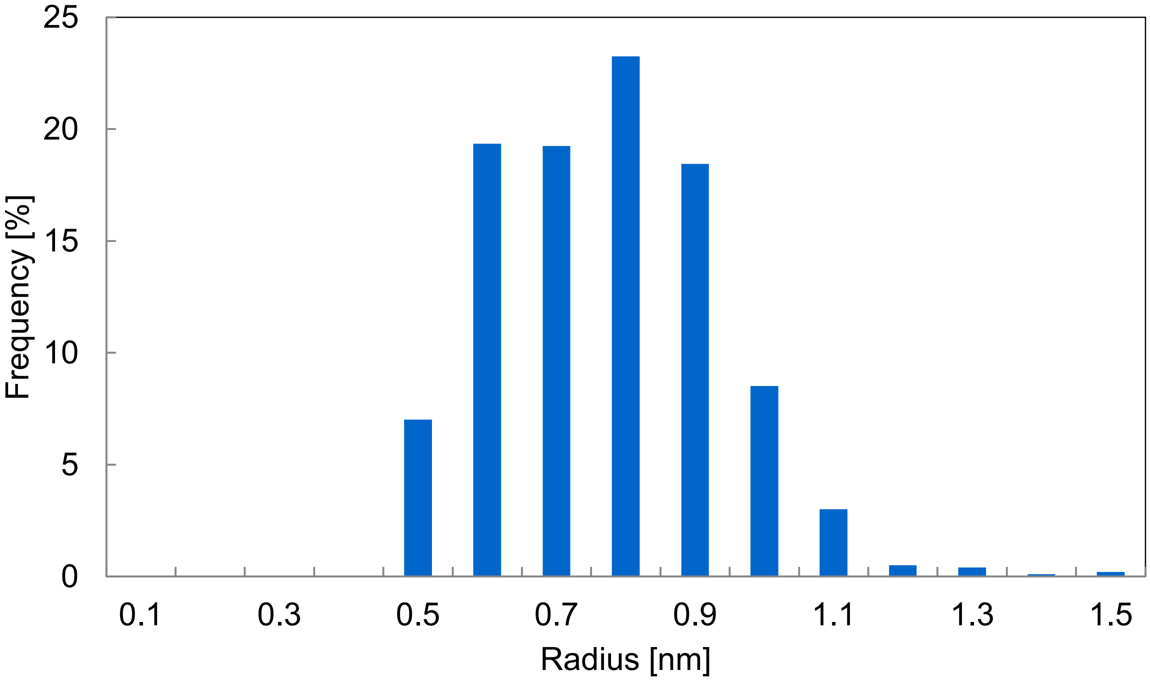

Figure 28. Size distribution of the precipitates in the aged and irradiated specimen.

The chemical composition of the precipitates and the matrix is given in Table 6. The precipitates are enriched in Ni, Al and Si, and depleted of Fe and Cr. Again, there still remain more than 30 at% Fe in the precipitates. A radial concentration profile based on the clusters depicted in Figure 27 was computed and is illustrated in Figure 29.

Table 6. Chemical composition in at% calculated with the cluster search algorithm for the aged and irradiated sample.

	Fe	Cr	Ni	Al	Mo	Mn	Si	C
Bulk	Bal.	12.4	8.98	3.69	0.82	0.37	0.66	0.02
		(±0.02)	(±0.02)	(±0.01)	(±0.005)	(±0.003)	(±0.004)	(±0.001)
Matrix	Bal.	13.05	6.69	2.71	0.92	0.34	0.51	0.03
		(±0.02)	(±0.01)	(±0.01)	(±0.005)	(±0.003)	(±0.004)	(±0.001)
Precipitates	Bal.	7.29	27.26	10.73	0.34	0.56	2.06	0.02
		(±0.02)	(±0.04)	(±0.03)	(±0.004)	(±0.006)	(±0.01)	(±0.001)

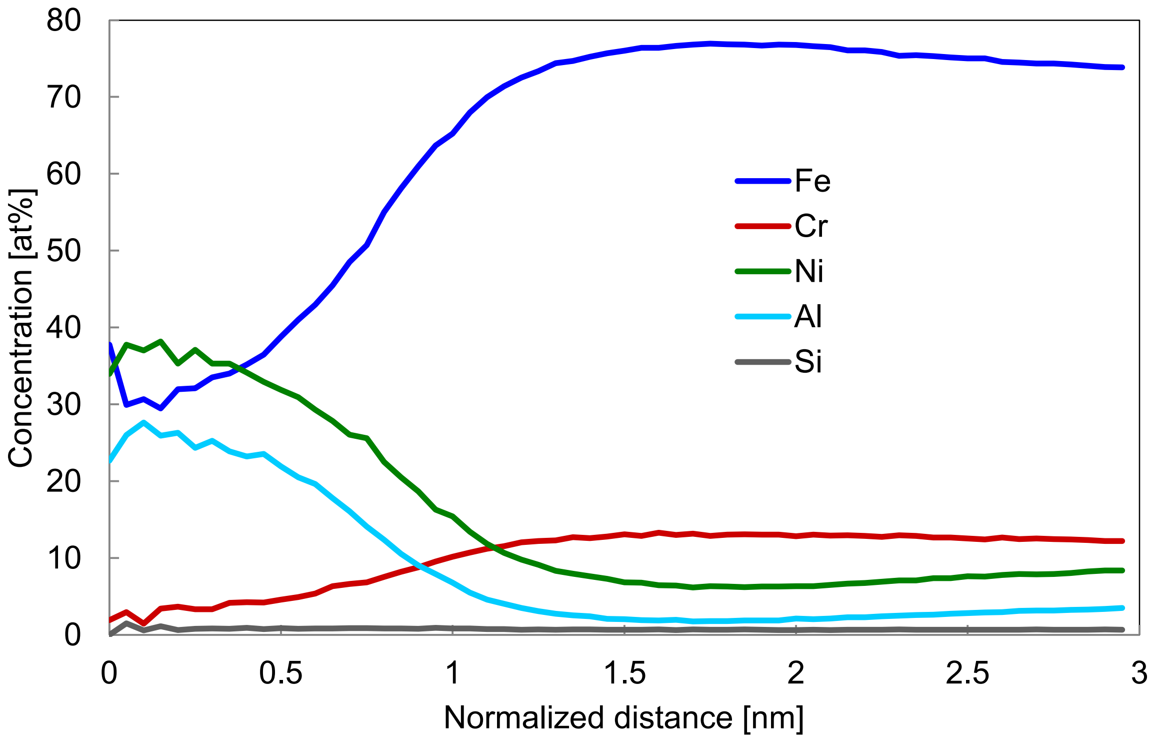

Figure 29. Radial concentration profile of the aged and irradiated sample based on the clusters depicted in Figure 27.

Figure 30 shows the radial concentration profile for the irradiated and unirradiated aged material for Ni, Al and Si. It is clearly evident that the Al content decreases from 25 at% to 20 at%, and the Si content increases significantly after irradiation.

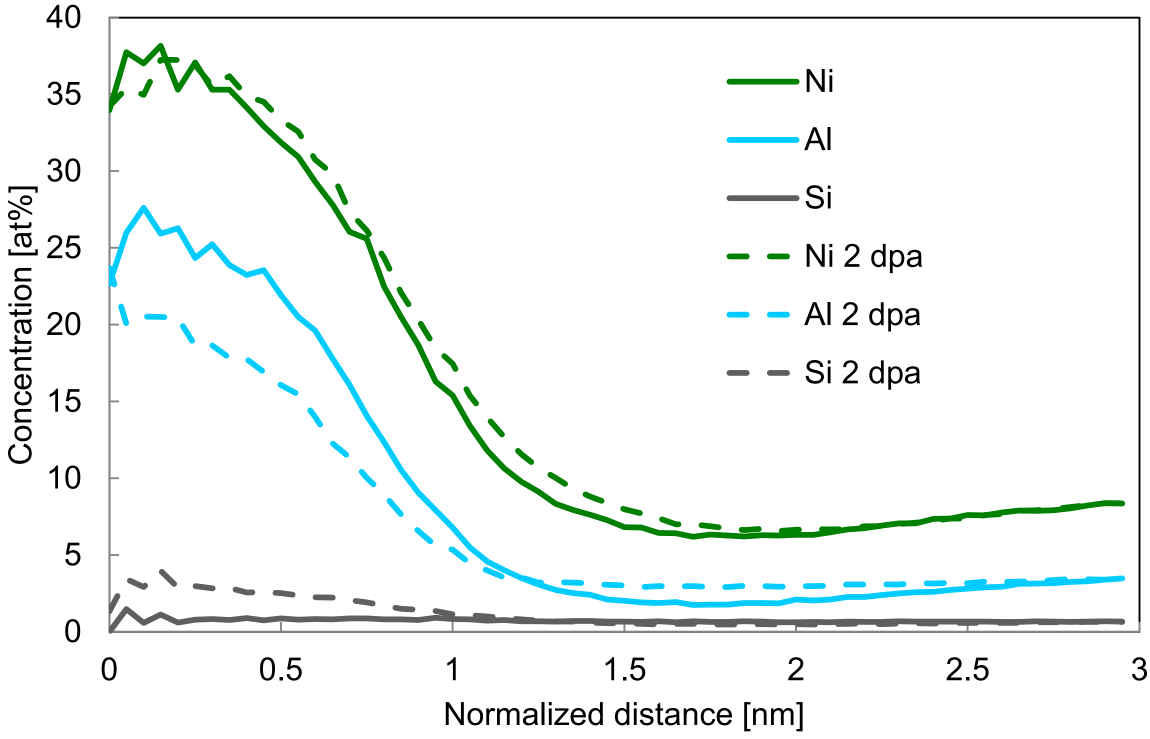

Figure 30. Comparison of the radial concentration profiles of the aged sample before and after irradiation.

4.5. Micro-compression testing

Micro-compression tests were performed on the solution annealed sample. The dimensions of the pillars were obtained in SEM mode in the dual-beam FIB prior to testing and are summarized in Table 7. The side-lengths of the pillars vary from 4 µm to 11.4 µm, what is taken into account by conversion of the load-displacement curves into engineering stress-strain curves according to equation (16) and (17). The distance from the edge was measured from the interface specimen / epoxy cold mount to the center of the pillars. Pictures of the pillars were acquired ante and post testing in the SEM mode. Pillar 2 in the unirradiated area and Pillar 1 in the irradiated area are exemplarily depicted in Figure 31.

Table 7. Dimensions of the micro-pillars, measured in the SEM mode.

	d_1 [µm]	d_2 [µm]	A [μm^2]	Height [µm]	Distance from the edge [µm]
Pillar 1, not irr.	10.0	10.0	100.00	14.22	-
Pillar 2, not irr.	9.5	6.1	57.95	12.00	-
Pillar 3, not irr.	7.8	6.0	46.80	13.10	-
Pillar 1, irr.	11.4	6.5	74.10	20.65	2.7
Pillar 2, irr.	10.7	6.1	65.27	20.65	4.1
Pillar 3, irr.	8.5	4	34.00	15.40	6.8

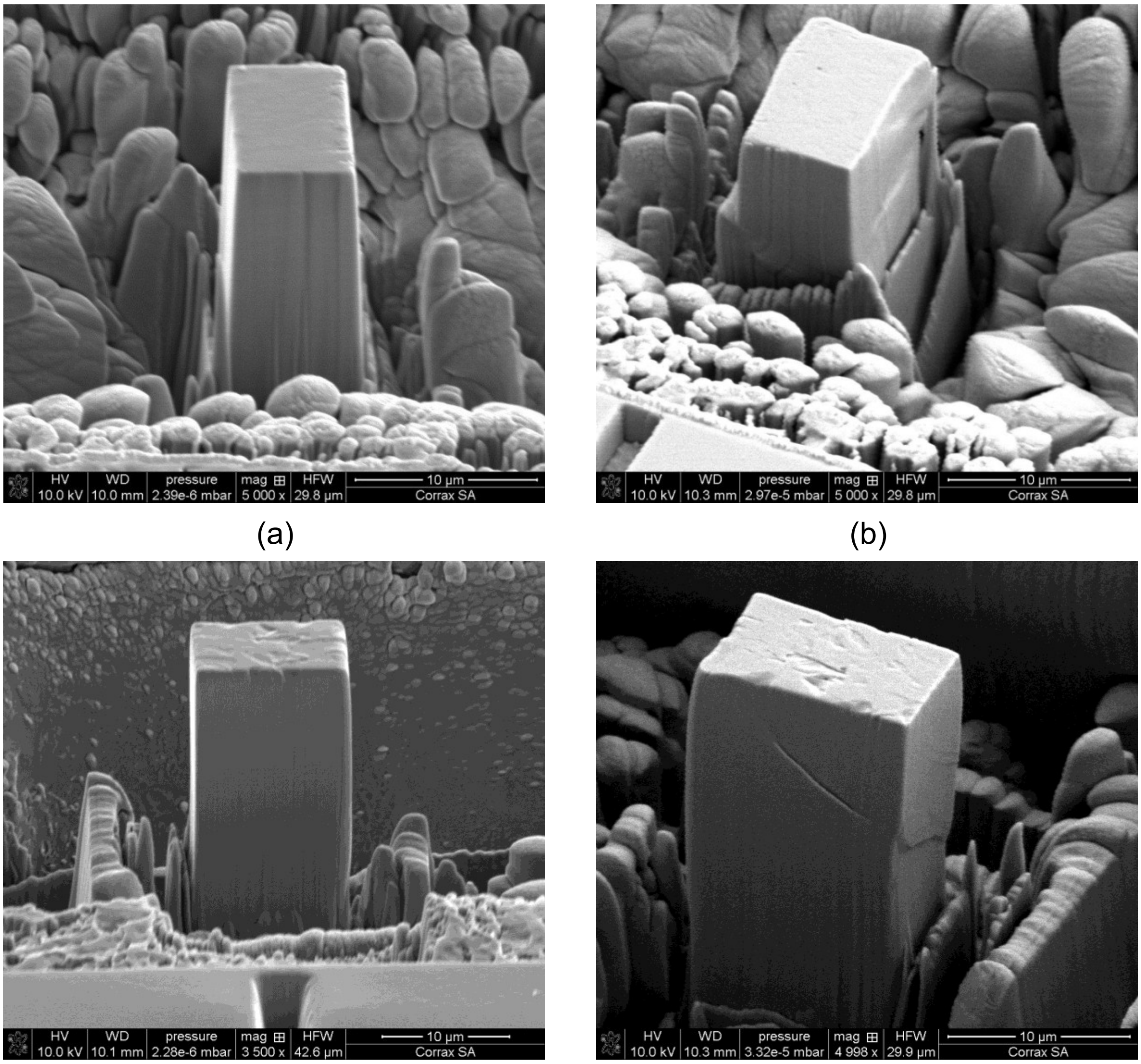

(a) (b)

(c) (d)

Figure 31. Pillar 2 in the unirradiated area (a) ante and (b) post testing and Pillar 1 in the irradiated area (c) ante and (d) post testing.

Figure 32 illustrates the engineering stress-strain curves for the unirradiated material. After the linear-elastic region all pillars exhibit work hardening up to stress values of about 1800 MPa, where the experiment was stopped to prevent destruction of the pillars. The curves for pillar 1 and pillar 3 look very similar, whereas it is apparent that pillar 2 shows higher strength.

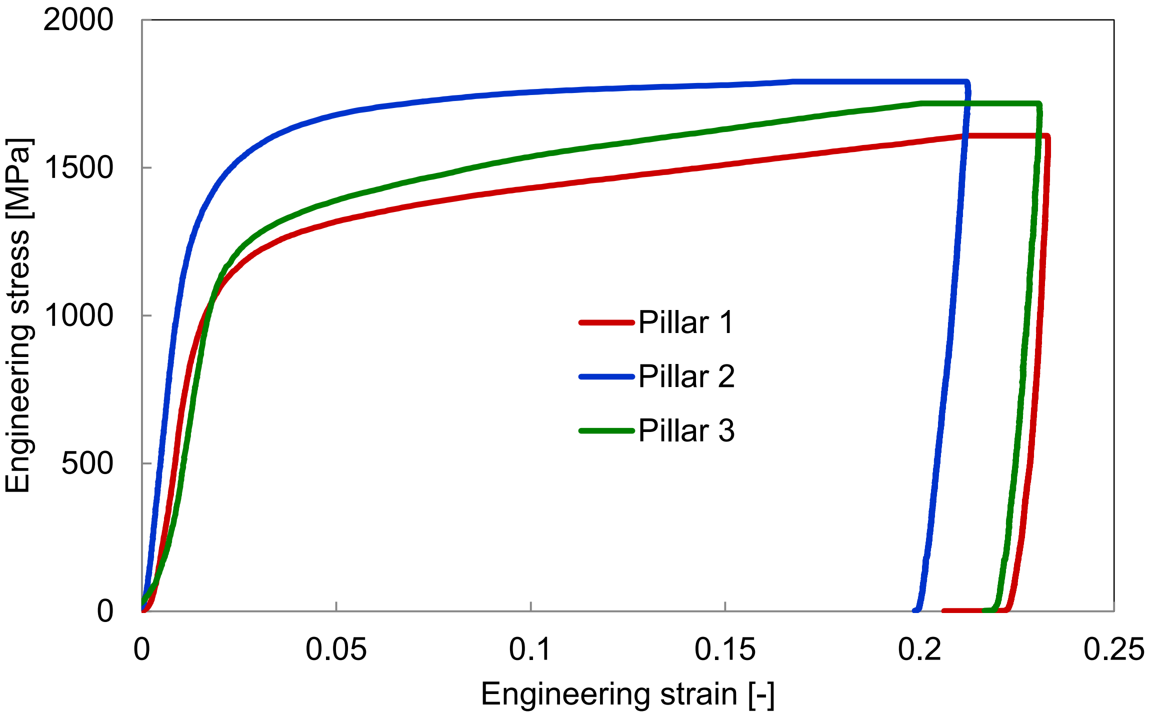

Figure 32. Stress-strain curves gained from micro-compression tests on PH 13-8 Mo in the solution annealed state on the not irradiated part.

Figure 33 depicts the pillars in the irradiated area post testing. Pillar 3 did not work out and the results could not be used. The red line indicates the interface to the epoxy cold mount. Pillar 1 and 2 are close to the edge, but pillar 4 is at the distance of the stopping peak and suffered a much higher dose rate.

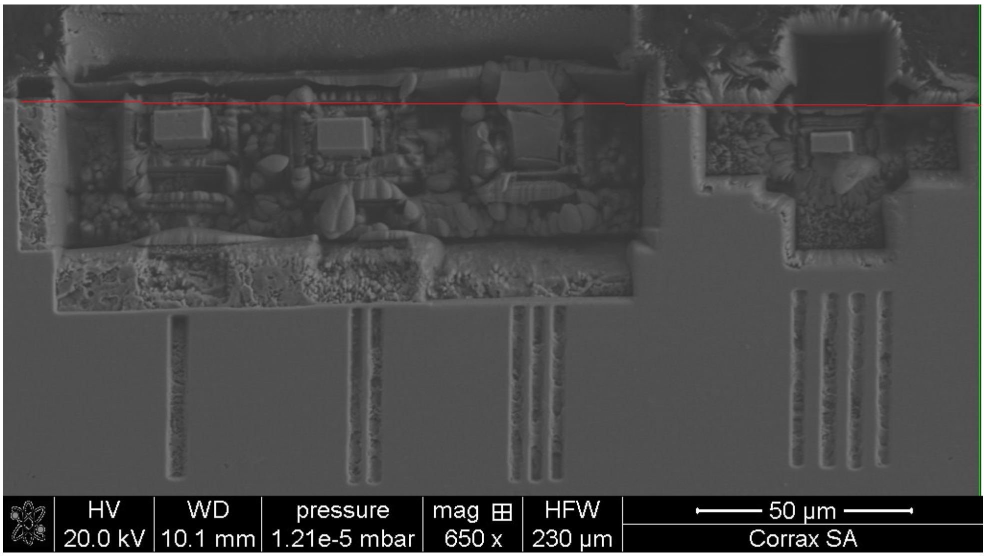

Figure 33. Top view of the pillars in the irradiated area post testing. The red line indicates the interface to the epoxy cold mount.

Engineering stress-strain curves for the pillars in the irradiated area are illustrated in Figure 34. Pillar 1 and pillar 2 exhibit similar behavior; after elastic deformation up to about 1700 MPa, they only show slight work hardening. Due to the fact that pillar 4 is located at the stopping peak, where the radiation damage is much higher, the increase in yield strength is more pronounced compared to pillar 1 and 2.

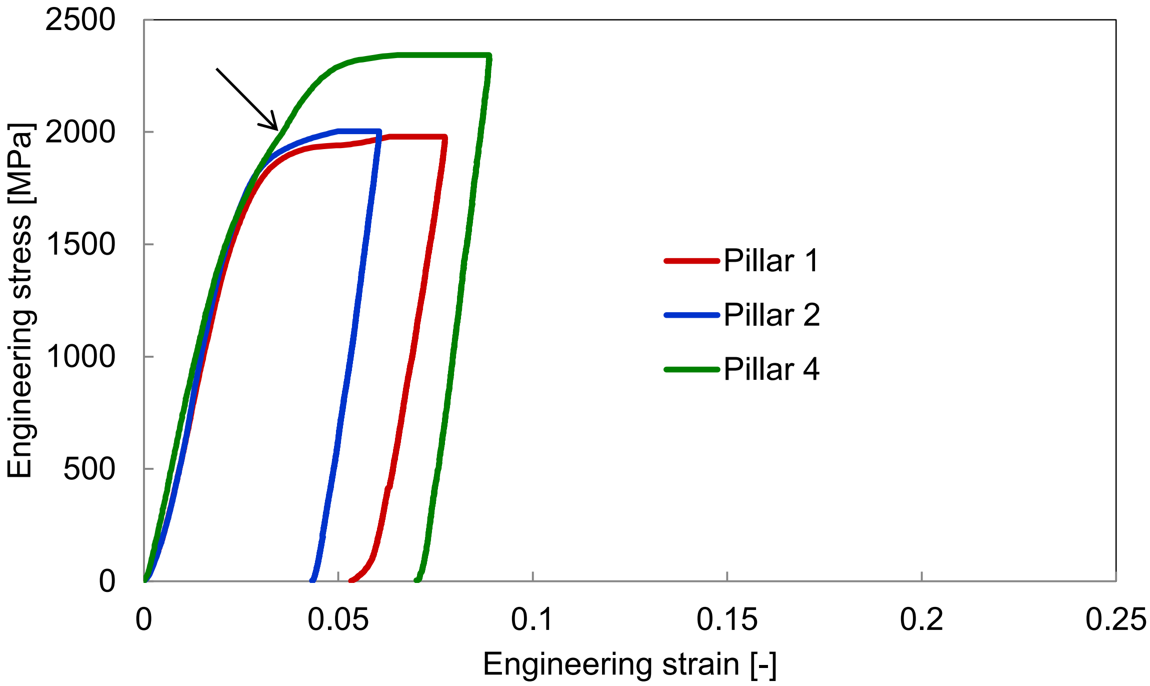

Figure 34. Engineering stress-strain curves gained from micro-compression tests on the irradiated area of the solution annealed sample.

The 0.2% offset yield stress under compression was determined for each pillar by parallel movement of the linear part of the loading curve by 0.002 of the engineering strain. This minimizes the influence of contact misfits occurring at the initial stage of loading. Results from the micro-compression tests are given in Table 8. The $R_{c0.2}$ value of pillar 4 underestimates the increase in strength because a deviation of the linear-elastic line around 1700 MPa occurs, indicated with an arrow in Figure 34, and therefore the offset yield stress cannot be accurately measured.

Table 8. 0.2% offset yield stress under compression of the micro pillars.

	Distance from the edge [µm]	$R_{c0.2}$ [N/mm^2]
Pillar 1, unirr.	-	990
Pillar 2, unirr.	-	1260
Pillar 3, unirr.	-	1160
Pillar 1, irr.	5.9	1660
Pillar 2, irr.	7.6	1730
Pillar 4, irr.	8.8	1650

In order to compare the strength increase measured with micro-compression tests and nanoindentation, the increase in strength due to nanoindentation was calculated according to the correlation proposed by Busby et al. [52]:

$$\Delta\sigma_y = 3.06 * \Delta H_v \tag{22}$$

ΔH_v is the increase in Vickers hardness in kg/mm^2 and $\Delta\sigma_y$ is the consequential increase in yield strength. The conversion of the hardness increase measured with nanoindentation into Vickers hardness was performed by applying equation (19). Pillar 4 in the irradiated material was excluded from the calculation because of its different radiation dose. Table 9 summarizes the changes in hardness and yield strength.

Table 9. Increase in yield strength due to irradiation on the solution annealed sample.

Measured ΔH (nanoindentation)	Calculated ΔHv	Calculated $\Delta\sigma_y$ (Busby)	Measured $\Delta\sigma_y$ (micropillars)
1.14 GPa	107.4 kg/mm^2	329 MPa	558 MPa

5. Discussion

The influence of proton irradiation on the mechanical properties and the precipitation kinetics of PH 13-8 Mo was investigated by means of nanoindentation, micro-compression testing and atom probe tomography. Comparison of the solution annealed condition and a condition aged for 2 h at 500°C before and after irradiation showed distinct differences in the material behavior and will be discussed separately.

5.1. Solution annealed condition

Performing nanoindentation on the cross section of a proton irradiated sample allows measuring the hardness changes as a result of irradiation. The hardness profile of the solution annealed condition, shown in Figure 16, exhibits a distinct hardness increase of 1.1 GPa of the irradiated material. The irradiated / unirradiated interface can be accurately measured and the stopping peak of the H^+ ions is apparent as well.

The hardness increase was also confirmed by micro-compression tests. Based on the engineering stress-strain curves, depicted in Figure 32 and Figure 34, the 0.2% offset yield stress under compression was determined. An average value of 1136 N/mm^2 was found for the yield stress of the unirradiated material, compared to an average yield stress of 1695 N/mm^2 of the irradiated material. As given in Table 9, the increase in strength obtained by micro-compression tests was also compared to the increase of strength estimated from nanoindentation according to Busby et al. [52]. The difference between the calculated yield strength increase, based on the nanoindentation measurements, and the experimentally observed one can have different reasons:

- The irradiated and unirradiated material exhibit a different indentation size effect because of their different intrinsic hardness [53].
- Micro-compression tests were designed for single crystals and the influence of the different orientations of the martensitic laths was not taken into account.
- Misalignment has a strong impact on the test accuracy, leading to a smearing of the transition from elastic-to-plastic deformation.

- Detrimental effects arise from dust particles on the sample or the flat-punch indentation tip, plastic buckling of the pillar and gallium implementation due to the fabrication in the FIB [3].

For clarification of the reason for the hardness increase, irradiated and unirradiated material were investigated by atom probe tomography. It can be seen in Figure 18 that all elements are homogenously distributed in the unirradiated condition. Visual inspection of the atom maps of Fe, Cr, Ni, Al and Si of the irradiated sample, provided in Figure 19, also leads to the assumption that all main elements are randomly distributed. However, frequency distribution analysis (Figure 20) shows a significant deviation from the binomial distribution, indicating that decomposition took place. The radial distribution function of Ni, shown in Figure 21, revealed zones enriched in Ni and Si and depleted of Fe and Cr.

An explanation for the decomposition could be radiation-enhanced diffusion. During irradiation a large number of point defects are generated. The stimulated diffusion can lead to defect aggregation or precipitation, depending on the balance between defect production rate and the loss of point defects to recombination or sinks [15].

In this work an attempt was made to calculate a diffusion coefficient during irradiation to evaluate if radiation-enhanced diffusion is a possible explanation for the occurring decomposition.

During irradiation a large amount of vacancies and interstitials are created. The behavior of these radiation-induced point defects depends on a large part on the amount of sinks in the material. A great number of sinks accomplishes that interstitials get caught in sinks before they have a chance to recombine with vacancies. Hence, after the point defect built-up, the concentration of vacancies C_v increases, while the interstitial concentration C_i decreases until both reach a quasi-steady state (Figure 35) [15]:

$$c_v^{SS} = -\frac{K_{is}C_s}{2*K_{iv}} + \left[\frac{K_0K_{is}}{K_{iv}K_{vs}} + \frac{K_{is}^2C_s^2}{4*K_{iv}^2}\right]^{\frac{1}{2}} \tag{23}$$

$$c_i^{SS} = -\frac{K_{vs}C_s}{2*K_{iv}} + \left[\frac{K_0K_{vs}}{K_{iv}K_{is}} + \frac{K_{vs}^2C_s^2}{4*K_{iv}^2}\right]^{\frac{1}{2}} \tag{24}$$

where

C_s = sink concentration

K_0 = defect production rate

K_{iv} = vacancy-interstitial recombination rate coefficient

K_{vs} = vacancy-sink reaction rate coefficient

K_{is} = interstitial-sink reaction rate coefficient

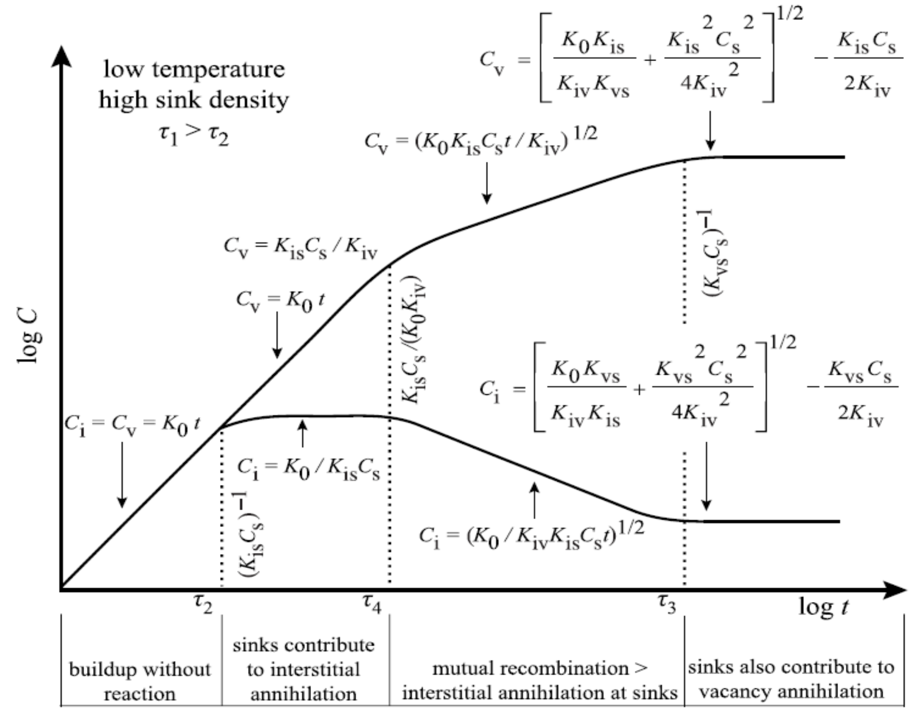

Figure 35. Vacancy and interstitial concentration plotted over the time for irradiation at room temperature and a high sink density [54].

The vacancy production rate K_0 is obtained from the SRIM calculation and amounts to $2.5*10^{18}$ vac/cm^3*s. The most important sinks in solution annealed PH 13-8 Mo are dislocations and, therefore, the dislocation density $\rho_D=10^{12}$ m^{-2} [55] is part of the equation for the sink concentration:

$$C_s = \frac{\rho_D}{a_0} \tag{25}$$

The interstitials and vacancies migrate by random walk diffusion, annihilating each other by mutual recombination or at unsaturable fixed sinks. Sinks and defects are assumed to be distributed homogeneously and no preferential absorption of specific point defects at specific sinks occurs. Therefore, the rate constants are as follows:

$$K_{iv} \approx 4 * \pi * r_{iv} * D_i \tag{26}$$

$$K_{is} = 4 * \pi * r_{is} * D_i \tag{27}$$

$$K_{vs} = 4 * \pi * r_{vs} * D_v \tag{28}$$

where r_{iv}, r_{vs} and r_{is} are interaction radii for the reaction between the species. R_{vs} and r_{is} were taken to be equal to the lattice parameter a_0, and r_{iv} is about twice as much [56].

The diffusion coefficient for vacancies depends on the number of nearest neighbors z, the diffusion mechanism and the crystal structure, both considered in the parameter A, the lattice constant a_0, and the jump frequency ω:

$$D_v = \alpha * a_0^2 * \omega \tag{29}$$

with

$$\alpha = \frac{1}{6} * z * A^2 \tag{30}$$

The jump frequency is the frequency with which an atom tries to break down the potential barrier between two equilibrium positions, generally assumed as the Debye frequency $v_D \approx 10^{13} s^{-1}$ multiplied with the Boltzmann factor, which takes into account the probability of success:

$$\omega = \nu * exp^{\left(\frac{S_m^v}{kT}\right)} * exp^{\left(\frac{-E_m^v}{kT}\right)} \tag{31}$$

The vacancy migration entropy can be neglected and therefore, the diffusion coefficient results in:

$$D_v = \alpha * a_0^2 * \nu * exp^{\left(\frac{-E_m^v}{kT}\right)} \tag{32}$$

with a vacancy migration energy of 0.68 eV [15]. The diffusion coefficient for interstitials D_i is calculated the same way as for vacancies with an interstitial migration energy of 0.33 eV [15].

The diffusion coefficient of lattice atoms is given by:

$$D_{rad} = D_v C_v + D_i C_i \tag{33}$$

The diffusion coefficient under irradiation added up to $3.21*10^{-18}$ cm^2/s. To set this value into proportion, a diffusion coefficient during heat treatment was calculated. The energy input during heat treatment also leads to a higher mobility of atoms due to an increase in the vacancy concentration. As a result to the enhanced diffusion precipitates are able to develop from the supersaturated solid solution [57].

The vacancy concentration during heat treatment results from the free vacancy formation energy G_f^v, the Boltzmann constant k, and the aging temperature T:

$$C_v = exp^{(\frac{-G_f^v}{kT})} \tag{34}$$

The free vacancy formation energy was taken to be 1.4 eV, the energy for vacancy formation in α-Fe [58].

The diffusion coefficient of lattice atoms by way of the vacancy mechanism is given by:

$$D_a = D_v C_v \tag{35}$$

For a body-centered material aged at 500°C for 2 h the diffusion coefficient accounts for $2.27*10^{-16}$ cm^2/s. This result agrees well with the diffusion coefficient for Fe in Fe diffusion of 10^{-16} cm^2/s in the literature [57].

The diffusion coefficient during irradiation is two orders of magnitude smaller than during heat treatment at 500°C for 2 h. This leads to the assumption that the diffusion is high enough to allow decomposition but still too weak for a full precipitation process. This theory is also backed up by the atom probe results, which show that after aging (Figure 22) distinct precipitates are detectable, whereas the element distribution still appears to be homogenous by visual inspection of the atom maps of Fe, Cr, Ni, Al and Si after irradiation of the solution annealed condition (Figure 19). Accompanied with the decomposition the hardness increased substantially. Similarly an increase in strength and embrittlement were detected in RPV steels after irradiation in consequence of the development of Cu clusters [16]. To gain more insight of the influence of the nominal composition on the precipitation kinetics of these clusters, a Cu-free Fe-1.1Mn-0.7Ni (at%) alloy was investigated [17]. Even there, decomposition enriched in Mn and Ni was found.

Guo et al. [12] also observed hardening effects during the initial stage of aging before detectable precipitates formed. They attributed this increase in hardness to the redistribution of atoms. Reich et al. [59] suggested a solute-dislocation interaction, where solute atoms segregate to existing dislocation causing dislocation locking.

Besides the decomposition also radiation-induced defects affect the hardness. The large amounts of vacancies and interstitials created during radiation can evolve to larger defects, e.g. dislocation loops [15]. Dislocation loops act as dispersed barriers for dislocation glide and therefore increase the yield strength. Transmission electron microscopy examination would be necessary to visualize them, but, this is beyond the scope of this work.

5.2. Aged condition

As can be seen in Figure 17, nanoindentation only revealed a very small increase in hardness due to irradiation in the sample aged at 500°C for 2 h. The precipitates formed during the aging treatment delayed the radiation damage. Van Renterghem et al. [22] suggested that existing precipitates in PH 13-8 Mo are not influenced by radiation because number density and radius do not change during irradiation. They attributed the hardness increase to the formation of dislocation loops. In this work, radius and number density are also comparable before and after irradiation, but the composition of the precipitates changes during the irradiation process. The radial concentration profile in Figure 30 revealed that the Al concentration decreased while the Si concentration increased in the precipitates due to irradiation. Zhang et al. [60] also detected a change in composition of Cu-rich precipitates after irradiation in a RPV steel. The concentration of Cu was found to significantly increase in the precipitates, indicating that irradiation leads to an approach to the equilibrium precipitate composition. According to that the radiation-enhanced diffusion should lead to an increase in the concentration of Ni and Al in the precipitates in irradiated PH 13-8 Mo approaching the equilibrium composition of NiAl. However, the Al concentration decreases considerably and Si enriches in the precipitates. Likewise, the clusters resulting from proton irradiation of the solution annealed condition exhibit a clear enrichment of Si, as illustrated in Figure 21. According to [61] NiAl has a solubility of over 10 at% for Si at 550°C, however, Si enrichment has not been detected before in NiAl precipitates in PH 13-8 Mo [13]. This might indicate that a change of precipitate type takes place. The reason for that could be that Si diffuses over a radiation-induced interstitial mechanism [62]. These results imply that there are differences in the precipitate evolution under proton irradiation and thermal aging.

It is clearly evident that the precipitates delay the materials degradation due to irradiation. It seems that precipitates act as recombination centers for both vacancy and interstitial defects. Ardell et al. [63] attributed the reduction of defect accumulation to the interaction of precipitates with dislocations. Another model [64] proposes that the elastic stresses arising around coherent precipitates force the recombination of point defects. This is questioned due to the low interaction between point defects and stress fields in general. Arokiam et al. [65] suggested that clusters of self-interstitials atoms created in displacement cascades become trapped inside precipitates and act as strong non-saturated sinks for vacancies.

Although it is still under discussion how coherent intermetallic precipitates influence the evolution of point defects, it appears to be a promising approach to further increase the radiation resistance of martensitic steels.

6. Summary

In this work the influence of proton irradiation on the precipitation kinetics and the resulting changes in mechanical properties of a PH 13-8 Mo maraging steel were investigated by means of nanoindentation, micro-pillar testing and atom probe tomography.

The nanoindentation results showed that in the solution annealed state a distinct hardness increase of 1.1 GPa due to irradiation occurred. Atom probe tomography revealed a decomposition of the main elements and zones enriched in Ni and Si were detected. This can be explained by the enhanced diffusion due to an increased amount of vacancies and interstitials produced during irradiation. In this work an attempt was made to calculate a diffusion coefficient during irradiation and set into proportion to the diffusion coefficient during aging. It turned out that the diffusion coefficient during irradiation is about two orders of magnitude lower than during aging at 500°C explaining why decomposition and not full precipitation occurred. The decomposed regions in combination with radiation induced defects such as dislocation loops are most likely responsible for the increase in hardness. Micro-compression tests also confirmed the increase in yield strength and correlate quite well with the estimation from nanoindentation.

As expected, the material aged for 2 h at 500°C only exhibited a small hardness increase of about 0.4 GPa. The large amount of defect sinks diminished the degradation of the material under irradiation. The number density and the radius are comparable before and after irradiation but the composition of the precipitates changes. It seems that a new precipitate type containing Ni, Al and Si developed. The interaction of coherent intermetallic precipitates and point defects produced during irradiation is still not fully understood, but it seems to be a promising approach to further increase the radiation resistance of martensitic steels.

References

1. G.S. Was et al., Emulation of neutron irradiation effects with protons: validation of principle, Journal of Nuclear Materials 300 (2002) 198-216.

2. W.C. Oliver, G.M. Pharr, Measurement of hardness and elastic modulus by instrumented indentation: Advances in understanding and refinements to methodology, Journal of Materials Research 19 (2004) 1564-1583.

3. M.D. Uchic, D.M. Dimiduk, A methodology to investigate size scale effects in crystalline plasticity using uniaxial compression testing, Materials Science and Engineering A 400-401 (2005) 268-278.

4. M.K. Miller, K.F. Russell, Atom probe specimen preparation with a dual beam SEM/FIB miller, Ultramicroscopy 107 (2007) 761-766.

5. G. Odette, M. Alinger, B. Wirth, Recent Developments in Irradiation-Resistant Steels, Annual Review of Materials Research 38 (2008) 471-503.

6. D.S. Gelles et al., Microstructural examination of commercial ferritic alloys at 200 dpa, Journal of Nuclear Materials 233-237 (1996) 293-298.

7. Y.A. Zot'ev et al., Radiation Resistance of Maraging Steel, Metallovedenie i Termicheskaya Obrabotka Metallov. 10 (1974) 43-45.

8. V. Seetharaman, M. Sundararaman, R. Krishnan, Precipitation Hardening in a PH 13-8 Mo Stainless Steel, Materials Science and Engineering 47 (1981) 1-11.

9. R. Taillard, A. Pineau, Room Temperature Tensile Properties of Fe-19wt.%Cr Alloys Precipitation Hardened by the Intermetallic Compound NiAl, Materials Science and Engineering 56 (1982) 219-231.

10. R. Taillard, A. Pineau, B.J. Thomas, The Precipitation of the Intermetallic Compound NiAl in Fe-19wt.%Cr Alloys, Materials Science and Engineering 54 (1982) 209-219.

11. R. Schnitzer, PhD Thesis, 'Structure-Properties Relationship of a Stainless Maraging Steel', Montanuniversität Leoben, Austria, 2010.

12. Z. Guo, W. Sha, D. Vaumousse, Microstructural evolution in a PH13-8 stainless steel after aging, Acta Materialia 51 (2003) 101-116.

13. M. Schober, R. Schnitzer, H. Leitner, Precipitation evolution in a Ti-free and Ti-containing stainless maraging steel, Ultramicroscopy 109 (2009) 553-562.

14. D.H. Ping, M. Ohnuma, Y. Hirakawa, Y. Kadoya, K. Hono, Microstructural evolution in 13Cr-8Ni-2.5Mo-2Al martensitic precipitation-hardened stainless steel, Materials Science and Engineering A 394 (2005) 285-295.

15. G.S. Was, 'Fundamentals of Radiation Materials Science',Springer Verlag Berlin, Heidelberg, 2007.

16. M.K. Miller, S.S. Brenner, FIM Atom Probe Study of Irradiated Pressure-Vessel Steels, Res Mechanica 10 (1984) 161.

17. E. Meslin, B. Radiguet, P. Pareige, A. Barbu, Kinetic of solute clustering in neutron irradiated ferritic model alloys and a French pressure vesel steel investigated by atom probe tomography, Journal of Nuclear Materials 399 (2010) 137-145.

18. M. Hernández-Mayoral, D. Gómez-Briceno, Transmission electron microscopy study on neutron irradiated pure iron and RPV model alloys, Journal of Nuclear Materials 399 (2010) 146-153.

19. J.M. Hyde et al., A comaprison of the structure of solute clusters formed during thermal ageing and irradiation, Ultramicroscopy 111 (2011) 664-671.

20. A.P. Druzhkov, D.A. Perminov, N.L. Pecherkina, Positron annihilation spectroscopy characterization of effect of intermetallic nanoparticles on accumulation and annealing of vacancy defects in electron-irradiated Fe-Ni-Al alloy, Philosophical Magazine 88 (2008) 959-976.

21. L.E. Steele, J.R. Hawthorne, R.A. Gray Jr., Neuron irradiation embrittlement of several higher strength steels, NRL Report 6419.1967.

22. W. Van Renterghem, A. Al Mazouzi, S. Van den Berghe, Defect structure of irradiated PH13-8Mo steel, Journal of Nuclear Materials 360 (2007) 128-135.

23. M. Jong, Characterization of PH13-8Mo after irradiation, NRG Report 21639/09.94111 (2009).

24. M. Jong et al., Post-irradiation charcterization of PH13-8Mo martensitic stainless steel, Journal of Nuclear Materials 417 (2011) 145-148.

25. D.A. Lucca, K. Herrmann, M.J. Klopfstein, Nanoindentation: Measuring methods and applications, CIRP Annals - Manufacturing Technology 59 (2010) 803-819.

26. P.M. Rice, R.E. Stoller, Materials Research Society Symposium Proceeding: 'Correlation of Nanoindentation and Conventional Mechanical Property', 2000.

27. W.C. Oliver, G.M. Pharr, An improved technique for determining hardness and elastic modulus using load and displacement sensing indentation experiments, Journal of Materials Research 7 (1992) 1564-1583.

28. A.C. Fischer-Cripps, 'The IBIS Handbook of Nanoindentation', Fischer-Cripps Laboratories Pty Ltd., Forestville, 2005.

29. M.S. De Guzman et al., The role of indentation depth on the measured hardness of materials, Materials Research Society Symposium Proceedings 308 (1993) 613-618.

30. E.W. Müller, The field ion microscope, Zeitschrift für Physik 42 (1951) 131-136.

31. T.F. Kelly, M.K. Miller, Atom probe tomography, Review of Scientific Instruments 78 (2007).

32. M.K. Miller, R.G. Forbes, Atom probe tomography, Materials Characterization 60 (2009) 461-469.

33. Böhler-Uddeholm, http://www.bucorp.com/corrax_p.htm, June 2011.

34. J.F. Ziegler, J.P. Biersack, U. Littmark, 'The Stopping and Range of Ions in Matter, SRIM', Pergamon, New York, 1985.

35. G.H. Pease, R.S. Kinchin, The Displacement of Atoms in Soldis by Radation, Reports on Progress in Physics 18 (1955) 1-51.

36. LANL, http://www.lanl.gov/mst/docs/LALP-06-036.pdf, August 2011.

37. The Wakasa Wan Energy Research Center, http://www.werc.or.jp/english/reseadeve/activities/accelerator/accelerator/tandem/index.htm, August 2011.

38. P. Hosemann et al., Nanoindentation on ion irradiated steel, Journal of Nuclear Materials 389 (2009) 239-247.

39. B.D. Beake, S.R. Goodes, J.F. Smith, Nanoscale materials testing under industrially relevant conditions: high-temperature nanoindentation testing, Zeitschrift für Metallkunde 94 (2003) 798-801.

40. Miller, M.K. Atom probe tomography. New York : Springer, 2000.

41. M.K. Miller, K.F. Russell, K. Thompson, R. Alvis, D.J. Larson. Review of Atom Probe FIB-Based Specimen Preparation Methods. Microscopy and Microanalysis. 2007, Vol. 13, pp. 428-436.

42. D.W. Saxey et al., Atom probe specimen fabrication methods using a dual FIB/SEM, Ultramicroscopy 107 (2007) 756-760.

43. P. Hosemann et al., Macro and microscale mechanical testing and local electrode atom probe measurements of STIP irradiated F82H, Fe-8Cr ODS and Fe-8Cr-2W ODS, Journal of Nuclear Materials (2011) in press.

44. I.N. Sneddon, The relation between load and penetration in the axisymmetric bussinesq problem for a punch of abitrary profile, International Journal of Engineering Science 3 (1965) 47-57.

45. C.A. Volkert, E.T. Lilleodden, Size effects in the deformation of sub-micron Au columns, Philosophical Magazine 86 (2005) 5567-5579.

46. J. Onoro, Martensite microstructure of 9-12%Cr steels weld metals, Journal of Materials Processing Technology 180 (2006) 137-142.

47. R. Schnitzer et al., Microstructural Characterization of PH 13-8 Mo Maraging Steels, Praktische Metallographie 46 (2009) 521-536.

48. M. Schober, R. Schnitzer, H. Leitner, Proc. 17th IFHTSE Congress, 'Microstructure Evolution during Aging of two different Stainless Maraging Steels', Kobe, 2009, 478-481.

49. R. Schnitzer et al., Influence of reverted austenite on static and dynamic mechanical properties of a PH 13-8 Mo maraging steel, Materials Science and Engineering A 527 (2010) 2065-2070.

50. P. Moody et al., Quantitative Binomial Distribution Analyses of Nanoscale Like-Solute Atom Clustering and Segregation in Atom Probe Tomography Data, Microscopy Research and Technique 71 (2008) 542-550.

51. V. Vaumousse, A. Cerezo, P.J. Warren, A procedure for quantification of precipitate microstructures from three-dimensional atom probe data, Ultramicroscopy 95 (2003) 215-221.

52. J.T. Busby et al., The relationship between hardness and yield stress in irradiated austenitic and ferritic steels, Journal of Nuclear Materials 336 (2005) 267-278.

53. W.D. Nix, H. Gao, Indentation size effects in crystalline materials: A law for strain gradient plasticity, Journal of the Mechanics and Physics of Solids 46 (1998) 411-425.

54. R. Sizemann, Journal of Nuclear Materials 69/79 (1987) 386-412.

55. E.V. Pereloma, A. Shekhter, M.K. Miller, S.P. Ringer, Ageing behaviour of an Fe-20Ni-1.8Mn-1.6Ti-0.59Al (wt%) maraging alloy: clustering, precipitation and hardening, Acta Materialia 52 (2004) 5589-5602.

56. M.P. Macht et al., Temperature-Dependent Sink Concentration in Ni and Cu, Physica Status Solidi A 104 (1987) 287-295.

57. G. Gottstein, 'Physikalische Grundlagen der Materialkunde', Springer-Verlag Berlin, Heidelberg, 2007.

58. S.M. Kim, W.J.L. Buyers, Vacancy formation energy in iron by positron annihilation, Metal Physics 8 (1987) 103-108.

59. L. Reich, S.P. Ringer, K. Hono, Origin of the initial rapid age hardening in an Al-1.7 at.% Mg-1.1 at.% Cu alloy, Philosophical Magazine Letters 9 (1999) 639-648.

60. Z.W. Zhang et al., Effects of proton irradiation on nanocluster precipitation in ferritic steel containing fcc alloying additions, Acta Materialia 60 (2012) 3034-3046.

61. V. Raghavan, Al-Ni-Si (Aluminium-Nickel-Silicon), Journal of Phase Equilibria and Diffusion 26 (2005) 262-267.

62. A. Etienne, B. Radiguet, P. Pareige, Understanding silicon-rich phase precipitation under irradiation in austenitic stainless steels, Journal of Nuclear Materials 406 (2010) 251-256.

63. A.J. Ardell, R.B. Nicholson, J.D. Eshelby, On the modulated structure of aged Ni-Al alloys, Acta Metallurgica 14 (1966) 1295.

64. D.A. Perminov, A.P. Druzhkov, V.L. Arbuzov, Role of intermetallic nanoparticles in radiation damage of austenitic Fe-Ni-based alloys studied by positron annihilation, Journal of Nuclear Materials 414 (2011) 186-193.

65. A.C. Arokiam, A.V. Barashev, D.J. Bacon, Y.N. Osetsky, Atomic-scale computer simulation study of the interaction of Cu-rich precipitates with irradiated-produced defects in alpha-Fe, Philosophical Magazine 87 (2007) 925-943.